Segmentation techniques for noisy MRI scans

Ksenia Slepova

TU Delft

Segmentation techniques for noisy MRI scans

by

Ksenia Slepova

to obtain the degree of
Master of Science
in Applied Mathematics
at the Delft University of Technology,
to be defended publicly on Wednesday August 30, 2023 at 10:30 AM.

Student number: 5634458
Thesis committee: Prof. dr. ir. M.B. van Gijzen, TU Delft, supervisor
Dr. ir. W. T. van Horssen, TU Delft

An electronic version of this thesis is available at http://repository.tudelft.nl/.

TU Delft

Abstract

Every year, 180,000 new cases of hydrocephalus are diagnosed among infants in Sub-Saharan Africa. Unfortunately, more than two-thirds of the population in this region lacks access to essential medical imaging technologies, such as magnetic resonance imaging (MRI). To address this issue, a collaborative effort between the TU Delft, Leiden University Medical Center, Penn State, and Mbarara University of Science and Technology has led to the development of a low-cost, portable, low-field MRI system. However, images obtained from this scanner are often noisy and distorted and might contain artefacts, therefore, need preprocessing before they can be utilized in diagnostics. The enhancement of their quality can be achieved through both hardware calibration and optimization, as well as the application of filtering, enhancement, and segmentation techniques. In this master's project, we propose a two-step PDE-based segmentation approach. Additionally, we compare it with the modified approach where presegmentation in the initial phase of the standard algorithm is introduced. Both approaches yield segmentation results comparable to the ground truth or manually performed segmentation. Nonetheless, there remains room for further improvement in both denoising and segmentation techniques.

Preface

A bit more than two years ago I moved to the Netherlands and started my masters in Applied Mathematics at the TU Delft. After these two years, I can confidently say that despite all the challenges I had to confront in both my everyday life and studies, this was undoubtedly one of the best decisions I've ever made.

When it came to choosing the master's project, I approached Martin van Gijzen and learned about this low-field MRI project. Since I had always aspired to apply my mathematical knowledge in ways that contribute to medical advancement, I decided to join Martin in this research. As I can say now, it was another decision that I am extremely happy about.

I would like to express my heartfelt gratitude to you, Martin, for your endless positivity and unwavering support at every step of this journey. I'm immensely thankful to Dr. Johnes Obungoloch, Ivan Etoku and the entire MUST MRI Lab team for the warm welcome in Mbarara and the incredible experience I gained during this visit.

My friends from Russia and Bulgaria, your constant (digital) support is priceless to me, thank you from the bottom of my heart. Sincere thanks to those, who I met in Delft and who became my friends during this captivating journey. I am incredibly grateful to my beloved one, Tsvetik, whose smile, care and understanding have given me strength to overcome all the difficulties I've encountered in recent months. And lastly, I express my deepest gratitude to my family, thank you for always being unconditionally by my side.

Ksenia Slepova
Delft, August 2023

Abbreviations and Acronyms

Abbreviation	Definition
$2D$	Two-dimensional
$3D$	Three-dimensional
ADMM	Alternating Direction Method of Multipliers
AHE	Adaptive Histogram Equalization
CSF	Cerebrospinal Fluid
CT	Computer Tomography
DPCG	Deflated Preconditioned Conjugate Gradient
FDM	Finite Difference Method
HE	Histogram Equalization
MRI	Magnetic Resonance Imaging
PCG	Preconditioned Conjugate Gradient
PDF	Probability Density Function
PET	Positron Emission Tomography
RF	Radiofrequency
SDAM	Squared Deviation from the Absolute Mean
SDCM	Squared Deviation from the Class Mean
SRG	Seeded Region Growing
TV	Total Variation

Contents

1

Introduction

Approximately 180,000 infants are diagnosed with hydrocephalus in Sub-Saharan Africa each year [1]. This is a congenital or acquired condition caused by accumulation of cerebrospinal fluid (CSF) resulting in abnormal expansion of the cerebral ventricles [2]. Inadequate diagnosis and poor treatment, which happen due to lack of specialized medical high technology equipment, might lead to severe brain damage and, ultimately, death.

The most effective tool of diagnosing this disease is Magnetic Resonance Imaging (MRI) [3]. MRI is a non-invasive imaging technology that produces three dimensional detailed anatomical images and is commonly used for disease detection, diagnosis, and tracking treatment progress [4].

However, MRI systems and their maintenance are expensive and not accessible in 66 % of the world [5]. According to the World Health Organizations recent statistics [5], 44 to 67% of the population in low- and lower-middle-income countries has poor availability of non-communicable diseases (NCD) tests/procedures relying on specific medical devices while this number for high-income countries is limited to 2%. Specifically, 40% of low-income and 27% of lower-middle-income countries do not have any units of MRI.

1.1. Motivation

In a recent joint project of the Technical University of Delft (TU Delft), Leiden University Medical Center (LUMC), Pennsylvania State University (PSU), and Mbarara University of Science and Technology (MUST) a prototype of an inexpensive and sustainable device has been designed [6, 7]. Later, a team of LUMC developed an updated version of the MRI

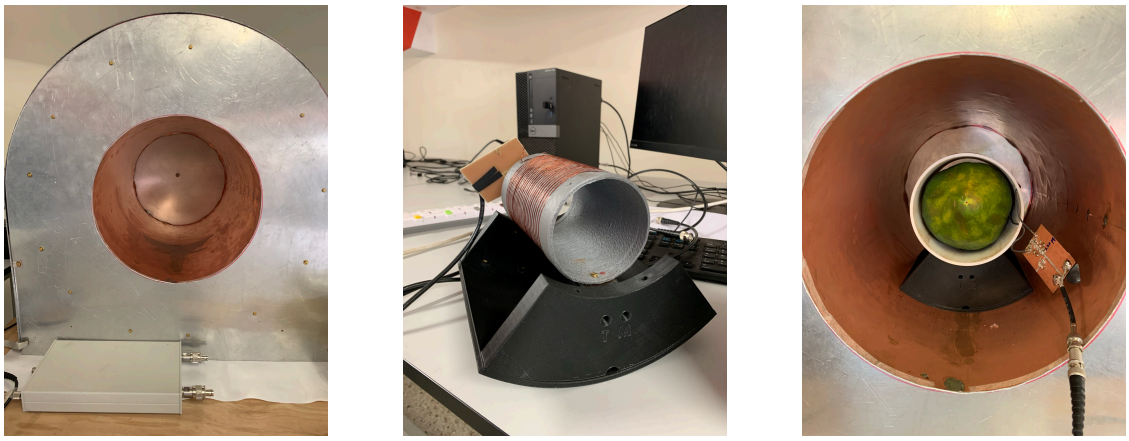

(a) (b) (c)

Figure 1.1: Low-field MRI scanner developed by the LUMC and the TU Delft. *Upper left image*: the scanner, *Upper right image*: the radio frequency (RF) coil, *Bottom image*: MUST MRI scanner during a measurement of a phantom (a papaya).

scanner, and its copy (see Figure 1.1) was constructed at MUST [8]. The latter is still under development, therefore, the image quality can still be improved by hardware optimizations. The approximate costs of this MRI system (excluding machining and personnel) sum up to around 13,500 euros while those of a conventional multipurpose whole-body MRI reach several million euros.

A cheaper point-of-care mobile MRI system should make testing for hydrocephalus more accessible to patients in Uganda. However, images obtained from this scanner are often noisy and distorted, and might contain artefacts, therefore, they should undergo pre-processing before being used in diagnostics.

1.2. Related Research

There has been a lot of research conducted on denoising and image enhancement for MRI scans and low-field MRI in particular. The University of Hong Kong research group has already studied many clinical patients, incorporating various noise removal and advanced image processing techniques [9, 10, 11]. Brown University's Advanced Baby Imaging Lab has already studied numerous cases of human subjects, with noise removal and segmentation into white matter, gray matter and CSF [12, 13, 14, 15]. The Rosen Lab has worked

on developing low-cost “purpose-built" MRI systems for brain imaging and enhancing obtained images [16, 17].

1.3. Research Questions

As mentioned above, although a low-field MRI system will provide many people with access to this type of medical diagnosis, scans obtained from it are frequently of poor quality. Nevertheless, both hardware and software improvements can be made in order to significantly increase it.

Research on enhancement and segmentation of low-field MR images is mainly focused on artificial intelligence (AI) techniques, as is exemplified by the work in the above references. This thesis focuses on analytical, PDE-based techniques. We follow the two-stage approach suggested in [18]. The idea behind the approach is to firstly find the approximation of the initial image by solving a minimization problem that includes image reconstruction and image filtering terms. In the second stage, several enhancing techniques and Jenks natural breaks classification method [19] are employed to obtain the final segmentation of the initially noisy MR scan. We aim to answer the following research questions:

1. Can a two-step PDE-based segmentation approach applied to noisy MR scans produce reliable results?

2. Can a two-step approach, extended by adding a presegmentation step, yield more accurate segmentation than standard one?

1.4. Report Outline

The report is structured in the following way: Chapter 1 contains introduction to the research topic. Next, in Chapter 2 and Chapter 3 respectively, image filtering techniques and standard segmentation methods are described. Additionally, Chapter 4 covers how the two-step segmentation approach can be applied to process noisy images. In Chapter 5 the basics of the MRI concepts are explained and the data set on which the numerical experiments are conducted is presented. Chapter 6 contains the results and the analysis of our model performance. Finally, Chapter 7 is devoted to the conclusions and Chapter 8 provides suggestions for future research.

2

Image Filtering Techniques

In this chapter we will discuss the model that we use as a filtering technique for a noisy or distorted images. Moreover, we will briefly and concisely describe the numerical discretization of the obtained system and the ways to solve it using Picard iteration and preconditioning.

2.1. Diffusion PDE's for noise reduction

The Perona-Malik diffusion model is a filtering technique that allows to reduce image noise without diffusing the edges or other significant image details [20, 21]. It is given by the equations below:

$$\frac{\partial u(\mathbf{x},t)}{\partial t} = \nabla \cdot (c(\|\nabla u(\mathbf{x},t)\|)\nabla u(\mathbf{x},t)) \quad \text{in } \Omega \times (0,T) \tag{2.1}$$

$$u(\mathbf{x},0) = f(\mathbf{x}) \quad \text{in } \Omega \tag{2.2}$$

$$\frac{\partial u(\mathbf{x},t)}{\partial \mathbf{n}} = 0 \quad \text{on } \partial\Omega \times (0,T). \tag{2.3}$$

Here Ω is the picture domain, T is the stopping time, $u(\mathbf{x},t)$ is the image intensity, f is an initial noisy image and c is a function satisfying following conditions:

- $c(\|\nabla u(\mathbf{x},t)\|)$ is a non-negative monotonically decreasing function,
- $\lim_{\|\nabla u(\mathbf{x},t)\|\to 0} c(\|\nabla u(\mathbf{x},t)\|) = M$, where $M \in (0,\infty)$,

- $\lim_{\|\nabla u(\mathbf{x},t)\|\to\infty} c(\|\nabla u(\mathbf{x},t)\|) = 0.$

The basic anisotropic diffusion PDE from Equation 2.1 can be modified in such a way that the updated equation maintains the fidelity to the original image, the stopping time does not have to be chosen anymore and the diffusion termination at trivial solutions, such as a constant image, is avoided (see [22]). Extra terms are added to the right-hand side which brings us to the following PDE:

$$\frac{\partial u(\mathbf{x},t)}{\partial t} = \nabla\cdot(c(\|\nabla u(\mathbf{x},t)\|)\nabla u(\mathbf{x},t)) + \eta(u(\mathbf{x},0) - u(\mathbf{x},t)) \quad \text{in } \Omega\times(0,T) \tag{2.4}$$

The added terms $\eta(u(\mathbf{x},0) - u(\mathbf{x},t))$ in Equation 2.4, with η being a fidelity parameter, are providing constraint that penalizes variation of the output image from the input one. Knowing the initial condition, $u(\mathbf{x},0)$ can be substituted with $f(\mathbf{x})$.

2.1.1. Diffusion Coefficients

The original model suggests the following diffusion coefficients:

$$c(\|\nabla u(\mathbf{x},t)\|) = \exp\left(-\left(\frac{\|\nabla u(\mathbf{x},t)\|}{K}\right)^2\right), \tag{2.5}$$

$$c(\|\nabla u(\mathbf{x},t)\|) = \frac{1}{1+\left[\frac{\|\nabla u(\mathbf{x},t)\|}{K}\right]^2}. \tag{2.6}$$

Despite their ability to sharpen edge, these coefficients are unable to remove heavy-tailed noise and create the so-called "staircase" artefacts. Although this "staircase" effect is not useful for image enhancement, it might be beneficial to segmentational purposes.

The following Gaussian-smoothed diffusion coefficient was proposed in to avoid the above-mentioned issues [23]:

$$c(\|\nabla u(\mathbf{x},t)\|) = \exp\left(-\left(\frac{\|\nabla u(\mathbf{x},t) * G_\sigma\|}{K}\right)^2\right), \tag{2.7}$$

where K is a damping parameter and G_σ is Gaussian filter with standard deviation σ.

Another option is a parameter-free total variation diffusion coefficient

$$c(\|\nabla u(\mathbf{x},t)\|) = \frac{1}{\|\nabla u(\mathbf{x},t)\|}. \tag{2.8}$$

Moreover, morphological operations (discussed later in Section 3.4) can be incorporated in the diffusion coefficients:

$$c(\|\nabla u(\mathbf{x},t)\|) = \exp\left(-\left(\frac{\|\nabla S(\mathbf{x},t)\|}{K}\right)^2\right), \tag{2.9}$$

where $S = (u(\mathbf{x},t) \bullet B) \circ B$ is the morphological closing-opening filter with B being a structuring element [24].

Finally, we consider the elastic net modification of the total variation diffusion coefficient:

$$c(\|\nabla u(\mathbf{x},t)\|) = \frac{1}{d_p} \cdot \left(\frac{1}{\|\nabla u(\mathbf{x},t)\|^2}\right)^{\frac{d_p}{2}-1} + K. \tag{2.10}$$

Here d_p is the diffusion power and K is the diffusion parameter.

2.2. Picard Iteration

We will consider the following model:

$$0 = \nabla \cdot (c(\|\nabla u(\mathbf{x})\|)\nabla u(\mathbf{x})) + \eta(f(\mathbf{x}) - u(\mathbf{x})) \quad \text{in } \Omega \tag{2.11}$$

It can be viewed as one time-step of implicit Euler method applied to Equation 2.1

$$\frac{u^1 - u^0}{\tau} = \nabla \cdot (c(\|u^1\|)\nabla u^1) \tag{2.12}$$

which can be rewritten using the known initial condition and by taking $\eta = \frac{1}{\tau}$ and $u = u^1$:

$$\nabla \cdot (c(\|u\|)\nabla u) + \eta(f - u) = 0. \tag{2.13}$$

Equation 2.13 exactly coincides with Equation 2.11. It can also be noticed that Equation 2.4 is a time-dependent form of Equation 2.11. In [25, Section 2.7.6], the authors explain that, under certain conditions, the solution $u(\mathbf{x},t)$ of the time-dependent problem should approximate a minimizer $u(\mathbf{x})$ of the model Equation 2.11 as time increases.

To solve the system, we firstly discretize Equation 2.11 in space using the standard finite difference method (FDM) (see, for instance, [20, 26]). In the two-dimensional case, we obtain the following semi-discrete system:

$$0 = C(\mathbf{u})\mathbf{u} + \eta(\mathbf{f} - \mathbf{u}), \tag{2.14}$$

where

$$\mathbf{u} = (u_{0,0}, \cdots, u_{N-1,0}, \cdots, u_{0,N-1}, \cdots, u_{N-1,N-1})^T, \tag{2.15}$$

$$\mathbf{f} = (f_{0,0}, \cdots, f_{N-1,0}, \cdots, f_{0,N-1}, \cdots, f_{N-1,N-1})^T, \tag{2.16}$$

and N is the number of subintervals in each direction. The system for the three-dimensional case can be derived similarly.

Rewriting Equation 2.16 brings us to the following form:

$$\left(1 - \frac{1}{\eta} C(\mathbf{u})\right)\mathbf{u} = \mathbf{f}. \tag{2.17}$$

The nonlinear system in Equation 2.18 is then solved using the lagged diffusion Picard iteration as suggested in [27]:

$$\left(1 - \frac{1}{\eta} C\left(\mathbf{u}^n\right)\right)\mathbf{u}^{n+1} = \mathbf{f}. \tag{2.18}$$

Denoting $A(\mathbf{u}) := \left(1 - \frac{1}{\eta} C(\mathbf{u})\right)$, $\mathbf{b} := \mathbf{f}$, we obtain the final linear system that needs to be solved in every Picard iteration:

$$A\left(\mathbf{u}^n\right)\mathbf{u}^{n+1} = \mathbf{b}. \tag{2.19}$$

2.3. Deflated Preconditioned Conjugate Gradient Method

Deflated Preconditioned Conjugate Gradient Method (DPCG), see e.g.[28], is a method allowing to speed up the convergence of the Preconditioned Conjugate Gradient Method (PCG) when applied to a number of problems [29, 30].

In Section 2.2 we discussed the numerical discretization and the final system that has to be solved in each Picard iteration. Matrix A in Equation 2.19 is symmetric and positive definite. However, discontinuities in the diffusion coefficient might occur resulting in A being ill-conditioned.

System Equation 2.19 can be solved using the conjugate gradient method. Moreover, it can be sped up by solving preconditioned system

$$M^{-1} A\mathbf{u} = M^{-1}\mathbf{b}, \tag{2.20}$$

where M is chosen in such a way that it resembles A. Further improvements in the speed of the convergence can be performed by applying deflated preconditioner (DPCG). This allows to map isolated eigenvalues to zero, effectively removing them from the system [31].

The projector P is defined as follows:

$$P = I - AZ(Z^T AZ)^{-1} Z^T, \quad Z \in \mathbb{R}^{n \times m}, \tag{2.21}$$

where $Z = \begin{bmatrix} z_1 & z_2 & \dots & z_m \end{bmatrix}$ is the deflation matrix of a full rank and I is the identity matrix.

The solution $\mathbf{u}$ can be split into two terms $\mathbf{u} = (I - P^T)\mathbf{u} + P^T\mathbf{u}$. Replacing P with its definition in the first term yields

$$(I - P^T)\mathbf{u} = Z(\underbrace{Z^T AZ}_{:=\tilde{A}})^{-1} Z^T A\mathbf{u} = Z\tilde{A}^{-1} Z^T A\mathbf{u} = Z\tilde{A}^{-1} Z^T \mathbf{b}. \tag{2.22}$$

Therefore, we only need to calculate the second term $P^T\mathbf{u}$. We solve the deflated system using the fact that $AP^T = PA$ and the PCG method:

$$PA\tilde{\mathbf{u}} = P\mathbf{b}. \tag{2.23}$$

After we find $\tilde{\mathbf{u}}$, we can obtain $P^T\mathbf{u}$ by multiplying $\tilde{\mathbf{u}}$ by P^T.

There exist different possible choices for the matrix Z: it can be constructed by segmenting the image into small images using different methods, for example, region growing, thresholding, same size patches. In our research, we use the approach that defines Z based on the domain decomposition [28]. Assume that the domain Ω is divided into m nonoverlapping subdomains Ω_i, $i = 1, \cdots, m$. Then each column z_i of the matrix Z is defined as:

$$\begin{cases} z_i = 1, & \text{on } \Omega_i, \\ z_i = 0, & \text{on } \Omega_j,\ j \neq i, \end{cases} \quad \text{for } i = 1, \cdots, m. \tag{2.24}$$

Such choice of Z is called subdomain deflation.

To conclude, the DPCG method lets us split the solution into two parts, one of which is in the range of the deflation subspace $\mathscr{R}(Z)$ and the other one is in its complement. Pseudo-code for the algorithm can be found in [32, p. 462]

3

Segmentation Techniques

In this chapter basic segmentation techniques and their application to the problem are presented. Additionally, global and adaptive histogram equalization processes that allow significant enhancement of image quality are described. It is mainly based on [33, Chapters 3, 9, 10]

3.1. Thresholding

Thresholding is the simplest image segmentation technique that is allowing to split the image into regions by analysing its intensity values [33, p.760 – 764].

Assume that there is an intensity histogram, corresponding to an image $f(x,y)$, consisting of light objects on a dark background. Therefore, the pixels of the fore- and background can be grouped into two main modes with a threshold value equal to some T. Then the segmented image, $g(x,y)$, is defined as:

$$g(x,y) = \begin{cases} 1, \text{ if } f(x,y) > T, \\ 0, \text{ if } f(x,y) \leqslant T. \end{cases} \tag{3.1}$$

This is an example of a single threshold. It can be generalized in the following way: let $\{T_1, \ldots, T_n\}$ be the set of threshold values (assume that there are $(n-1)$ types of light objects

on a dark background). Then the segmented image, $g(x,y)$, is as follows:

$$g(x,y) = \begin{cases} a_1, & \text{if } f(x,y) > T_n, \\ a_2, & \text{if } T_{n-1} < f(x,y) \leqslant T_n, \\ \dots & \\ a_{n-1}, & \text{if } T_1 < f(x,y) \leqslant T_2, \\ a_n, & \text{if } f(x,y) \leqslant T_1, \end{cases} \tag{3.2}$$

where $\{a_1, a_2, \dots, a_n\}$ are n distinct intensity values. However, dual (or higher level) thresholding is difficult to solve, therefore, other techniques are preferable in such cases.

3.2. Edge Detection

In Section 2.1 we have already discussed filtering technique that allows to perform denoising of the image without diffusing the edges. It is given by Equation 2.4, Equation 2.10.

Once anisotropic diffusion has been applied to the initial image, edge detection procedure can be defined. The gradient magnitude $\|\nabla u(\mathbf{x})\|$ serves as such detector. Defining a certain threshold T of $\|\nabla u(\mathbf{x})\|$ gives us the locations of the edges $\mathbf{e}$:

$$\text{if } \|\nabla u(\mathbf{x})\| > T \Rightarrow \mathbf{e}(\mathbf{x}) = 1, \tag{3.3}$$

$$\text{if } \|\nabla u(\mathbf{x})\| \leqslant T \Rightarrow \mathbf{e}(\mathbf{x}) = 0. \tag{3.4}$$

For example, in the case of the diffusion coefficients from eqs. (2.5) and (2.6), parameter K can be used as such threshold. Indeed, for the small values of $\|\nabla u(\mathbf{x}, t)\|$ the diffusion flux arises, while for the large ones it is suppressed:

$$\text{if } \|\nabla u(\mathbf{x}, t)\| \ll K \Rightarrow c(\|\nabla u(\mathbf{x}, t)\|) \to 1, \tag{3.5}$$

$$\text{if } \|\nabla u(\mathbf{x}, t)\| \gg K \Rightarrow c(\|\nabla u(\mathbf{x}, t)\|) \to 0. \tag{3.6}$$

3.3. Background Removal Using Region Growing

Since the objects in MRI scans are generally center-located and the background is usually black, it can be subtracted from the image letting the foreground be extracted for further processing. *Seeded region growing*, originally presented in [34], is one of the techniques used for background removal. It is an algorithm performing a segmentation of an image

with respect to a set of seeds. The final result of the algorithm is an image split into regions satisfying the following requirements:

1) $\bigcup_{i=1}^{n} \Omega_i = \Omega$,

2) $\Omega_i \cap \Omega_j = \emptyset,\ i \neq j$,

3) Ω_i is a connected region, $i = 1,2,\ldots,n$,

4) $P(\Omega_i) = TRUE,\ i = 1,2,\ldots,n$,

5) $P(\Omega_i \cup \Omega_j) = FALSE,\ \forall i,j$ s.t. Ω_i, Ω_j are adjacent.

Here $P(\Omega_i)$ is some logical predicate defined over each Ω_i. For example, it might define some properties that should be met by each pixel within Ω_i.

In the first step, each region $\Omega_i,\ i = 1,2,\ldots,n$, consists of an initials set of seeds (a set might also consist of a single point). On each of the following steps, one pixel is added to one of the existing sets. The process of assigning a pixel to a set is as follows: consider the sets $\Omega_i,\ i = 1,2,\ldots,n$, after a certain step M. Let T denote the set of all unallocated for this moment pixels which border at least one of $\Omega_i,\ i = 1,2\ldots,n$:

$$T = \left\{ x \notin \bigcup_{i=1}^{n} \Omega_i \setminus N(x) \cup \bigcup_{i=1}^{n} \Omega_i \neq \emptyset \right\}, \tag{3.7}$$

where $N(x)$ denotes a set of immediate neighbors of the pixel x.

- If for $x \in T$ an intersection of $N(x)$ is non-empty with only one set Ω_i, then the index $i(x) \in 1,2,\ldots,n$ is defined as the one that gives $N(x) \cap \Omega_{i(x)} \neq \emptyset$. Moreover, we define a measure of differentness $\delta(x)$ of a pixel x from the region that it is assigned to as:

$$\delta(x) = |G(x) - \underset{y \in \Omega_{i(x)}}{\text{mean}}[G(y)]| \tag{3.8}$$

  with $G(x)$ being a gray value of the pixel x.

- If $N(x) \cap \Omega_i \neq \emptyset$ for more than one index, then $i(x)$ is chosen as the one that meets the condition of $N(x) \cap \Omega_{i(x)} \neq \emptyset$ and $\delta(x)$ is minimized.

After that, the $(M+1)$-th step is completed. The procedure continues until every pixel is allocated to one of the sets.

3.4. Morphological Operations

Before we introduce several *morphological operations*, let us give a few definitions. The translation of a set B by point $z = (z_1, z_2)$ is a set $(B)_z$ s.t.

$$(B)_z = \{b + z |\ b \in B\}. \tag{3.9}$$

Morphological operations have two inputs: an image that is to be processed and the second is a structuring element (SE), another, typically much smaller, image. The function of the structuring elements is to probe the input image. The SE can be of any shape, however, rectangles and circular regions of specified sizes are commonly employed.

Using the above notation, we can define the two morphological operations *dilation* and *erosion* [33, p. 652 – 657], [35, p. 78 – 79]. Let A, B be sets in Z^2. The *erosion* of A by structuring element B is defined as

$$A \oplus B = \bigcap_{b \in B} (A)_{-b}. \tag{3.10}$$

An example of an eroded image is presented in Figure 3.1.

(a) Input image.

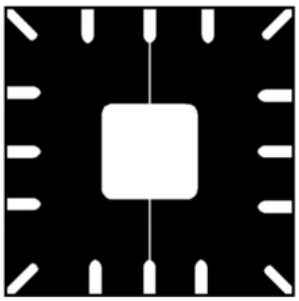

(b) Erosion by SE of size 11 × 11.

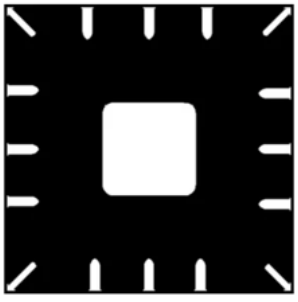

(c) Erosion by SE of size 15 × 15.

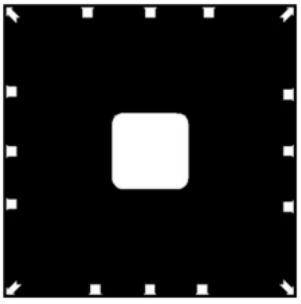

(d) Erosion by SE of size 45 × 45.

Figure 3.1: Example of erosion process with different sizes of structuring elements (SE) [33, p. 654].

The *dilation* of A by structuring element B is defined as

$$A \oplus B = \bigcup_{b \in B} (A)_b. \tag{3.11}$$

An example of dilated image is shown in Figure 3.2.

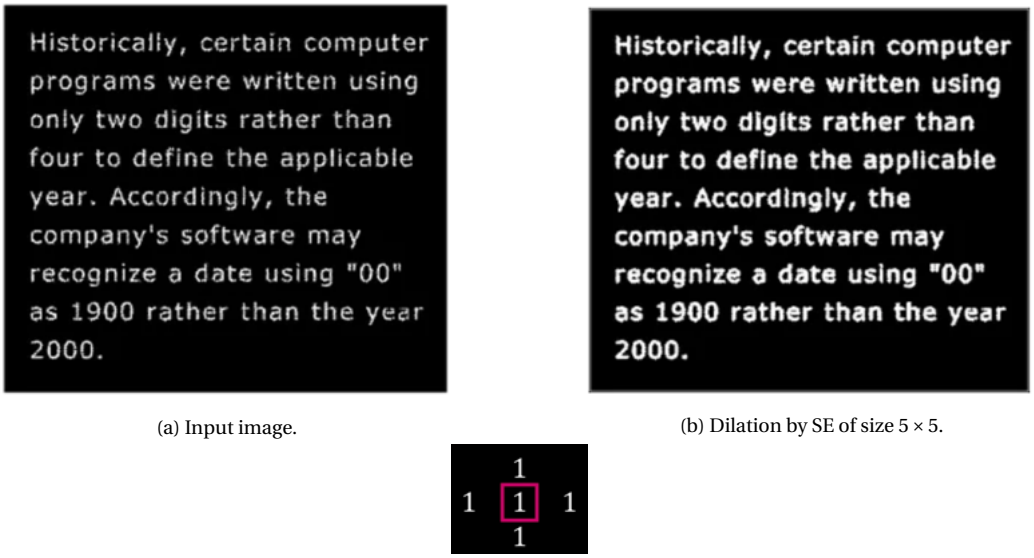

(a) Input image.

(b) Dilation by SE of size 5×5.

(c) Structuring element.

Figure 3.2: Example of dilation process with a structuring element Figure 3.2c [33, p. 656].

In other words, erosion allows removal of small-scale details from a binary image. Unlike erosion, which is frequently considered a thinning operator, dilation is used to fill in the holes in the existing image, thus, it can be thought of as a thickening operator that can, for instance, fill the existing holes.

Next, two more useful operations can be defined [33, p. 657 – 663]. The *opening* of a set A by structuring element B is

$$A \circ B = (A \ominus B) \oplus B. \tag{3.12}$$

The *closing* of a set A by structuring element B is

$$A \bullet B = (A \oplus B) \ominus B. \tag{3.13}$$

Using the above-mentioned operations, morphological filtering can be performed by applying opening followed by closing. In Figure 3.3 structuring element (B) of size 3×3 is used.

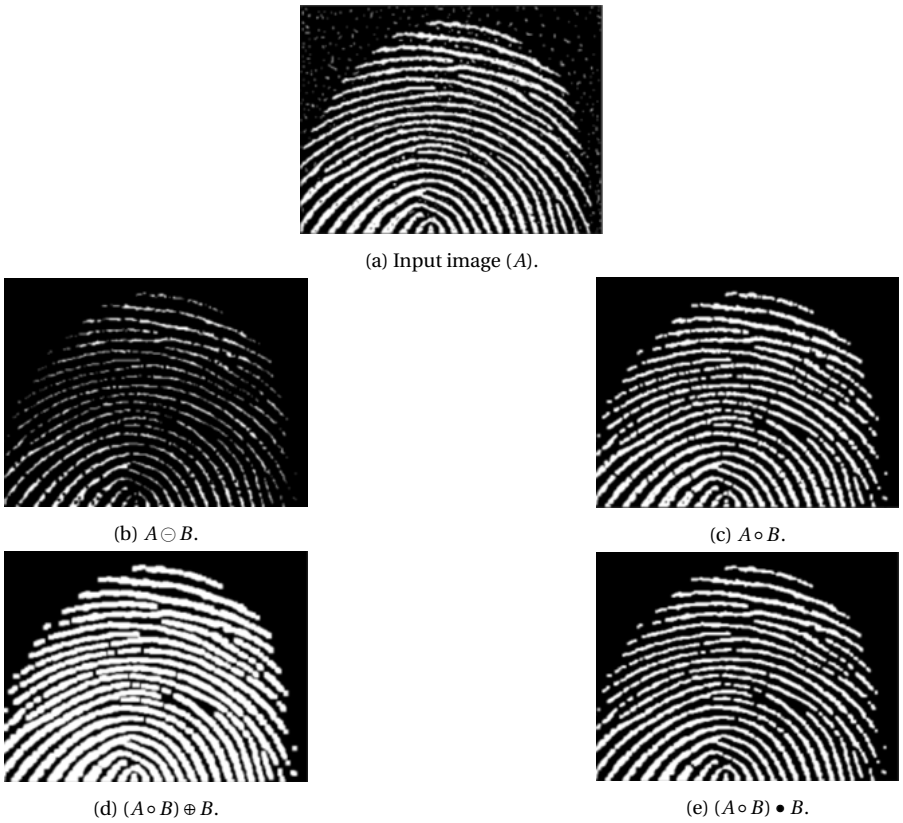

(a) Input image (A).

(b) $A \ominus B$.

(c) $A \circ B$.

(d) $(A \circ B) \oplus B$.

(e) $(A \circ B) \bullet B$.

Figure 3.3: Example of opening followed by closing [33, p. 661].

Finally, erosion and set difference can be used to extract object boundaries [33, p. 664]. Let the boundary of a set A be denoted as $\beta(A)$. Then it can be obtained as

$$\beta(A) = A - (A \ominus B), \tag{3.14}$$

where B is a suitable SE (see example in Figure 3.4).

3.5. Histogram Equalization

Histogram equalization is an image pre-processing method allowing to spread the intensity level of an initial image in such a way that the equalized image covers a wider range of the intensity scale, and, as a result, leading to contrast enhancement [33, p. 142 – 148].

Let r denote the intensities of the input image and let it be in the range $[0, L-1]$, where

(a) Input image. (b) Processed image.

Figure 3.4: Example of boundary extraction with a structuring element of size 3×3 [33, p. 665].

$r = 0$ stand for black and $r = L-1$ represents white. The histogram of an image is then a discrete function $h(r_k) = n_k$ with r_k being the k-th intensity value and n_k being the total number of pixels of the image with this specified intensity r_k. Therefore, if M and N are the row and column dimensions of the image, then the normalized histogram can be given by:

$$p_r(r_k) = \frac{h(r_k)}{MN} = \frac{n_k}{MN}, \; k = 0,1,2,\ldots,L-1. \tag{3.15}$$

Here MN gives the total number of the pixels in the image. Then the following transformation is called *histogram equalization*:

$$s_k = T(r_k) = (L-1)\sum_{j=0}^{k} p_r(r_j) = \tag{3.16}$$

$$= \frac{(L-1)}{MN}\sum_{j=0}^{k} n_j \quad k = 0,1,2,\ldots,L-1. \tag{3.17}$$

The idea behind it is that the probability density function (PDF) of s (the output image) has uniform distribution. Thus, such image will have an appearance of high contrast and will display a large variety of gray tones. An example of the output images obtained by histogram equalization are presented in Figure 3.5.

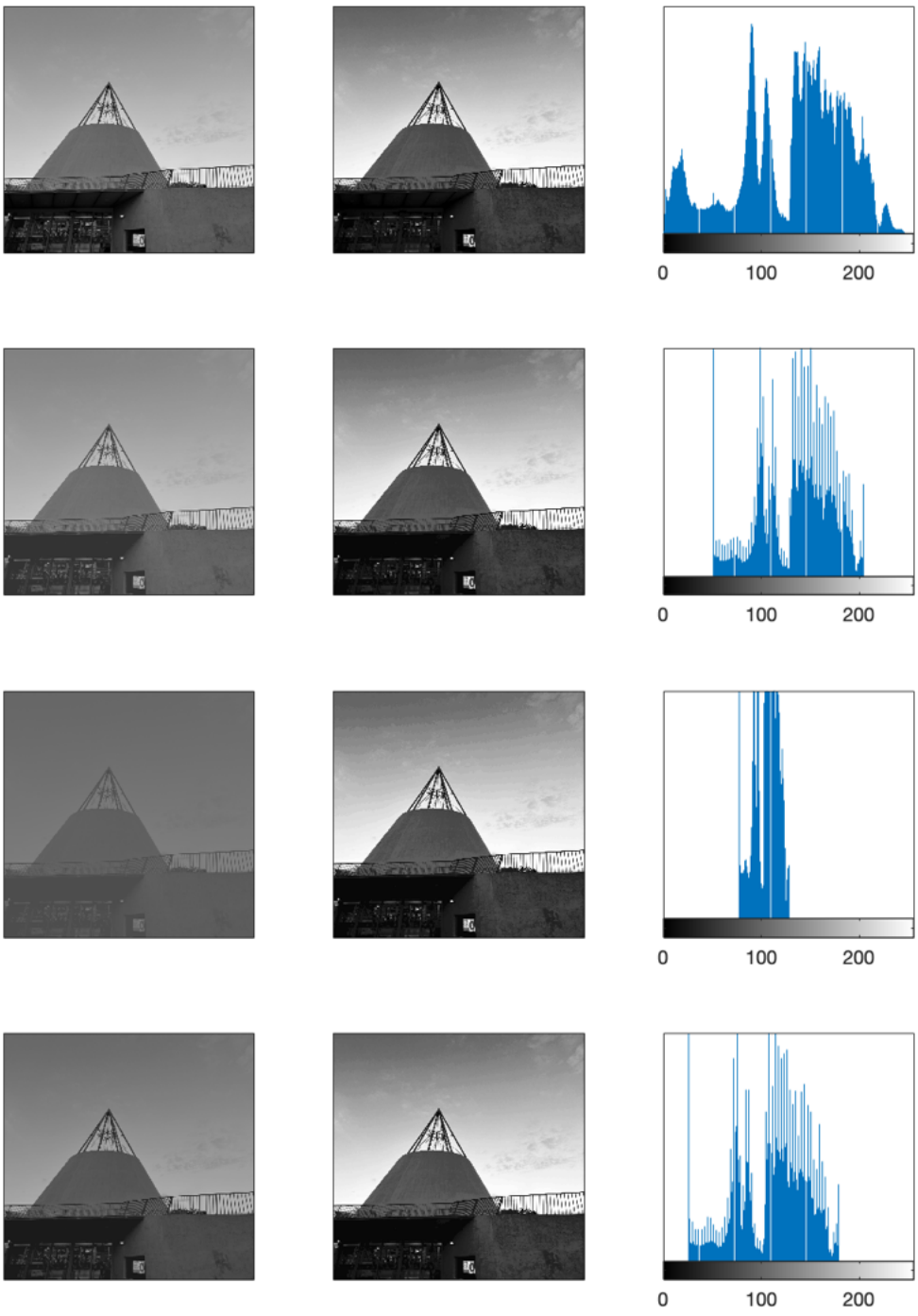

Figure 3.5: *Left column*: original input images, *middle column*: ouput of HE procedure, *right column*: corresponding histograms [33, p. 151]. These examples were performed by using `histeq` function in MATLAB.

3.6. Adaptive Histogram Equalization

The process discussed in Section 3.5 can be referred to as global histogram equalization since its transformation is based on the PDF of an entire image. Although in most of the cases it significantly increases the overall quality of an image, there are examples in which certain details should be enhanced over smaller parts of an image.

Considering local transformations, as mentioned in [33, p. 161], instead of global ones can serve as a possible solution to this issue. This approach is called *adaptive histogram equalization* (AHE). We will use its variation which was firstly suggested in [36]. Let an image have the size $M \times N$ and let us split it into contextual regions of the size $p_x \times p_y$. This implies that the total number of such regions, or patches, is as follows:

$$n_{\text{total}} = n_x \cdot n_y, \tag{3.18}$$

$$n_x = \frac{M}{p_x}, \tag{3.19}$$

$$n_y = \frac{N}{p_y}, \tag{3.20}$$

where n_x, n_y denote the number of patches in $x-$ and $y-$directions respectively.

For each of the patches, we compute its transformation function as in Equation 3.17:

$$s_{k_q} = \frac{(L-1)}{p_x \cdot p_y} \sum_{j=0}^{k} n_{j_q} \quad k = 0, 1, \cdots, L-1, \qquad q = 1, \cdots, n_{\text{total}}. \tag{3.21}$$

Moreover, we store the coordinates of the central pixels x_c and y_c for every patch:

$$x_{c_q} = x_{0_q} + \left\lfloor \frac{p_x + 1}{2} \right\rfloor \tag{3.22}$$

$$y_{c_q} = y_{0_q} + \left\lfloor \frac{p_y + 1}{2} \right\rfloor, \tag{3.23}$$

where x_{0_q} and y_{0_q} are global coordinates of the upper left corner pixel of the patch.

Once all the above-mentioned transformations are computed, we can perform adaptive equalization. The resulting mapping at any pixel is computed as a bilinear interpolation of the mapping at the four neighbouring pixels (see Figure 3.6). Consider a pixel with intensity j located at (x, y) and let $s_{j_{+-}}$ be the mapping of the patch to the upper right of (x, y). Similarly, $s_{j_{++}}$, $s_{j_{-+}}$, $s_{j_{--}}$ denote the mappings of the patches to the upper left, bottom left and bottom right respectively of (x, y). Then the result of the AHE is given by:

$$T_{\text{ahe}}(j) = c_y \left(c_x s_{j_{--}} + (1 - c_x) s_{j_{+-}} \right) + (1 - c_y) \left(c_x s_{j_{-+}} + (1 - c_x) s_{j_{++}} \right), \tag{3.24}$$

where

$$c_x = \frac{x - x_{c--}}{x_{c+-} - x_{c--}},\ c_y = \frac{y - y_{c+-}}{y_{c++} - y_{c+-}}. \tag{3.25}$$

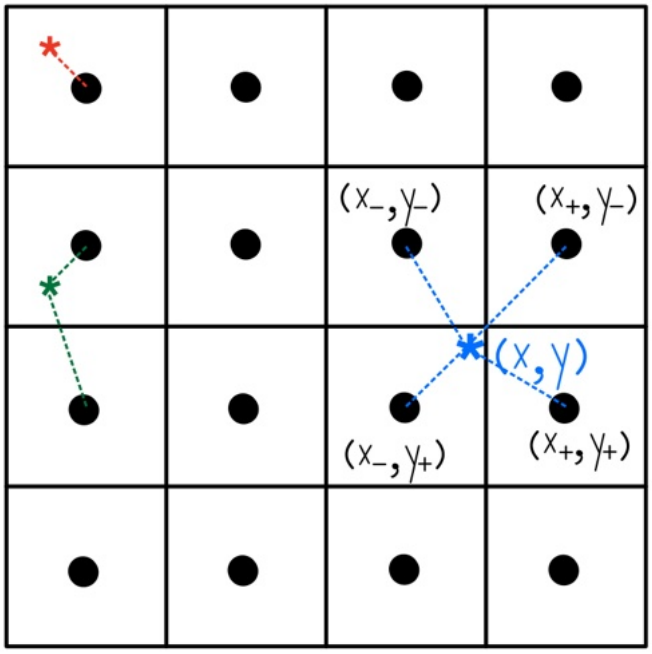

Figure 3.6: Example of sample points (·) for mapping computations and evaluation points (∗) (in the corner, at the border and between the four sampling points). Dashed line shows which neighbouring sample points are used for computing the AHE result of a particular pixel.

Mappings of the pixels located in the borders of the image should be computed specially, using linear interpolation of the two closest patches or, in case of the corner location, applying only one transformation.

Equalization process for the three-dimensional case can be derived in a similar way, adding trilinear interpolation to it.

3.7. k-means Clustering

The main idea of *k-means clustering method* is to give a partition of the initial set into k disjoint clusters (with k being a predefined parameter) [37]. In our research, we use the Jenks natural breaks classification method, which is a variation of the *k-means clustering method* but applied to univariate data [19]. This is an iterative process that consists of the following steps:

1. Choose the maximum number of clusters $n_{\text{cl.}}$;
2. Split the set into k initial clusters in some way which can be arbitrary;
3. Calculate the sum of squared deviations from the class means (SDCM);
4. Regroup the data into new clusters, possibly by moving elements from one cluster to a different one;
5. Compute new sum of deviations per cluster.

Steps 3, 4 and 5 are repeated until a certain tolerance τ is achieved or SDCM becomes constant.

Let us specify the way in the set is divided into clusters and which stopping criterion is used in our research. Firstly, all the pixel values are sorted and the number of clusters k is set to 1. After that, SDCM is computed. Moreover, the sum of squared deviations from the mean of the whole dataset (SDAM) and the goodness of variance fit (GVF) are calculated. The number of clusters is iteratively increased and the elements are moved from one class to another while

$$k < n_{\text{cl.}} \text{ and } \text{GVF} = \frac{\text{SDAM} - \text{SDCM}}{\text{SDAM}} < \tau.$$

4

Two-step Segmentation Approach

This chapter is devoted to the two-step segmentation approach and its application in our study. It was inspired by the paper of T. Wu *et al.* [18]. In this paper they introduced two-stage segmentation approach using non-convex $\ell^2 - \ell^p$ approximation of the Mumford-Shah (MS) model [38]. In the first step, they use the Split-Bregman algorithm to obtain the solution of a non-convex variant of MS model. In the second step, the obtained solution is segmented by applying thresholding in combination with the k-means clustering. In our research, anisotropic diffusion filtering is employed in the first step to enhance the image. Furthermore, splitting of the solution into clusters is performed with the Jenks natural breaks classification method. Additionally, we propose modification of the approach where the diffusion is based upon the segmented image.

4.1. Two-step Image Segmentation

Consider the following minimization problem:

$$\arg\min_{u} \frac{\eta}{2} \int_{\Omega} (f-u)^2 \, dx + R(\|\nabla u\|^2). \tag{4.1}$$

Here η is a fidelity parameter, u is an optimal approximation of the initial image f, $\Omega \subset \mathbb{R}^2$ is the image domain. Moreover, Ω is supposed to be a bounded open set with Lipschitsz boundary and f is continuous inside the image domain. Note that f is the result of model-based reconstruction of MRI signal. The second term is the regularization term. It should filter out noise while preserving the edges of the objects.

The energy functional given by Equation 4.1 is minimized by the solution of the corresponding Euler-Lagrange equations:

$$\nabla \cdot \big(R'(\|\nabla u\|)\nabla u\big) + \eta(f-u) = 0. \tag{4.2}$$

One can notice that it coincides with earlier derived Equation 2.11 because $R'(\cdot)$ is equal to the diffusion coefficient $c(\cdot)$. Detailed discussion of possible choices for $c(\cdot)$ can be found in Subsection 2.1.1. In Table 4.1 we present only total variation (TV) regulariser and the its extension with elastic net. The latter is used in our experiments.

Name	$R(s)$	$R'(s) = c(s)$
Total Variation	$2\sqrt{s}$	$\frac{1}{\sqrt{s}}$
Total Variation with Elastic Net	$s^{\frac{d_p}{2}} + Ks$	$\frac{1}{d_p} \cdot \left(\frac{1}{s}\right)^{\frac{d_p}{2}-1} + K$

Table 4.1: Choice of regularisers. Note that $s = \|\nabla u\|^2$.

Image reconstruction and filtering can be combined in one optimization problem since $R(\cdot)$ can serve as a regulariser for f as well:

$$\min_{f,u} \big[h(f) + g(u)\big] \quad \text{s.t. } u - f = 0. \tag{4.3}$$

Here

1. Image reconstruction is given by: $h(f) = \frac{1}{2}\|\mathscr{A} f - b\|_2^2$; $\min_f \big[h(f)\big]$;
   $\mathscr{A}$ is the Fourier transform [39];
2. Nonlinear diffusion filtering is represented by: $g(u) = \lambda R(\|\nabla u\|^2)$; $\min_u \big[g(u)\big]$;
   λ is the regularization parameter.

The method has two stages. In the *first stage* minimization problem Equation 4.3 is solved, thus, approximation u is obtained. In order to perform that, we use a single step of the *Alternating Direction Method of Multipliers* (ADMM) [40,].

In the *second stage* we perform splitting of the solution u into clusters. The authors of [18] proposed to use a combination of k-means clustering method (Section 3.7) and thresholding (Section 3.1). The solution u is firstly scaled in such a way that $\tilde{u} \in [0,1]$, thus, the

range of the smoothed data is restricted. Cluster centroids are denoted as c_i, $i = 1,2,\ldots,k$, and, without loss of generality, can be assumed to have intensities $\tilde{\rho}(c_1) \leqslant \tilde{\rho}(c_2) \leqslant \cdots \leqslant \tilde{\rho}(c_k)$. The thresholds are then computed as

$$\rho_i = \frac{\tilde{\rho}(c_i) + \tilde{\rho}(c_{i+1})}{2}, \quad i = 1,2,\ldots,k-1. \tag{4.4}$$

Afterwards, the scaled solution $\tilde{u}$ can be split into clusters by

$$\Omega_i := \{\mathbf{x} \in \Omega : \rho_{i-1} \leqslant \tilde{u}(\mathbf{x}) < \rho_i\}, \quad i = 1,2,\ldots,k. \tag{4.5}$$

Based on the idea of Wu *et al.*, we use the following two-step approach:

1. First step: enhance the image using anisotropic diffusion filtering with elastic net as a diffusion coefficient;
2. Second step: segment the image using background removal, morphological closing, global/adaptive histogram equalization and the Jenks natural breaks classification method.

4.2. Modified Two-step Approach

In the original two-step approach the diffusion coefficient is computed on basis of the original image. A new idea that we will investigate in Section 6.2 is to compute the diffusion on the segmented image instead . The motivation of this approach is that for segmentation we want sharp jumps in the diffusion coefficients.

Then the algorithm of the modified approach is as follows:

1. First step:
   - Perform segmentation of the unfiltered image using the Jenks natural breaks classification method;
   - Enhance previously segmented image using anisotropic diffusion filtering with elastic net as a diffusion coefficient;
2. Second step: segment the filtered image using background removal, morphological closing, global/adaptive histogram equalization and the Jenks natural breaks classification method.

5

MRI Measurements and Dataset

In this chapter we will give a brief introduction into MRI operation principle, mainly based on [41, Chapter 5]. Additionally, we will describe the data set that will be used for testing the proposed methods.

5.1. MRI operation principle

Magnetic resonance imaging (MRI) is a non-invasive diagnostic tool that produces detailed layer-by-layer images of almost any part of the human body, including, for instance, the muscles, blood vessels and organs. It is an example of medical application of nuclear magnetic resonance. MRI produces a visual representation of the spatial distribution of hydrogen nuclei (found in water and lipids) across different tissues. The image's brightness is determined by the quantity of protons present at each spatial point and the physical characteristics of the tissue, including its thickness, rigidity, and protein content. The key difference from other medical imaging methods, such as computer tomography (CT), positron emission tomography (PET), X-ray, is that no harmful radiation is required. MRI is extensively used for diagnosing various conditions, including neurological ones. Apart from being able to provide anatomical structure, MRI can be used to visualize blood flow (angiography), water diffusion, and localized brain activity.

The MRI system consists of three core hardware components: a superconducting magnet, a set of three magnetic field gradient coils, and a radio frequency transmitter and receiver (see Figure 5.1). Depending on the strength of the superconducting magnet used, MRI systems can be classified into several types [42, 43]:

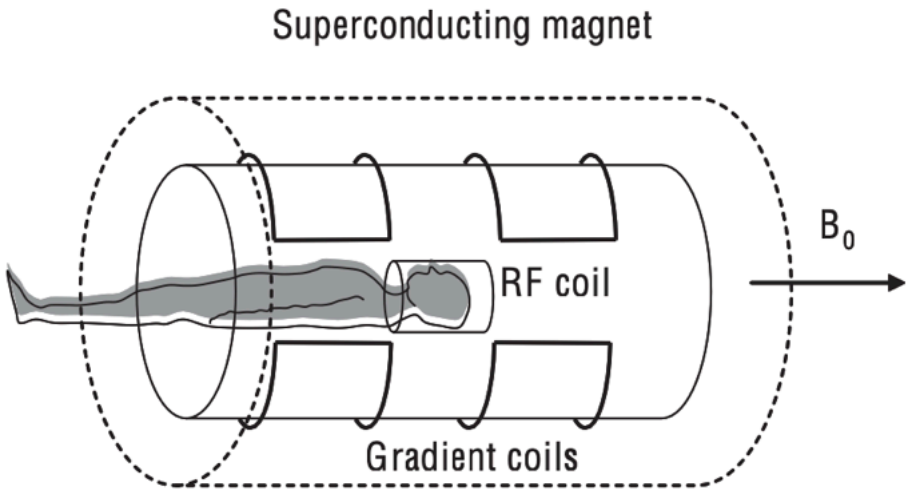

Figure 5.1: Major components of an MRI system. $\mathbf{B_0}$ denotes the magnetic field produced by the superconducting magnet [41, p. 205].

- ultra-low field (lower than 0,25 T);
- low-field (0,25 – 1 T);
- high-field (1 – 7 T);
- ultra-high field (higher than 7 T);

Exposed to this magnetic field, protons start precessing at a 'resonance' frequency, i.e., at a frequency proportional to the strength of the magnetic field. Moreover, adding the magnetic field gradients leads to this resonance frequency being dependent upon the spatial location of each proton in the body. This makes the image formation possible. Finally, a tuned radiofrequency (RF) coil serves as transmitter and/or receiver. It transmits the energy to the tissue, and same or other RF coil receives the induced MRI signal.

Let us discuss more in details the physics of MRI. As mentioned earlier, the hydrogen nucleus (a single proton) is contained in the water and other tissues of the human body. This single proton carries a positive electric charge [44]. The hydrogen protons are behaving like small magnets and are constantly spinning. Without external magnetic field applied to them, they have random orientation. Application of an external magnetic field aligns the protons either parallel or perpendicular to this field.

This alignment can be disturbed by applying RF pulses that make the protons flip and rotate. The duration of such pulses typically counts to few microseconds. After the RF pulses are switched off, the nuclei return to their equilibrium state, releasing energy that can be measured (a signal). It is this signal that is then used for an MR image to be created [45].

5.2. Dataset Description

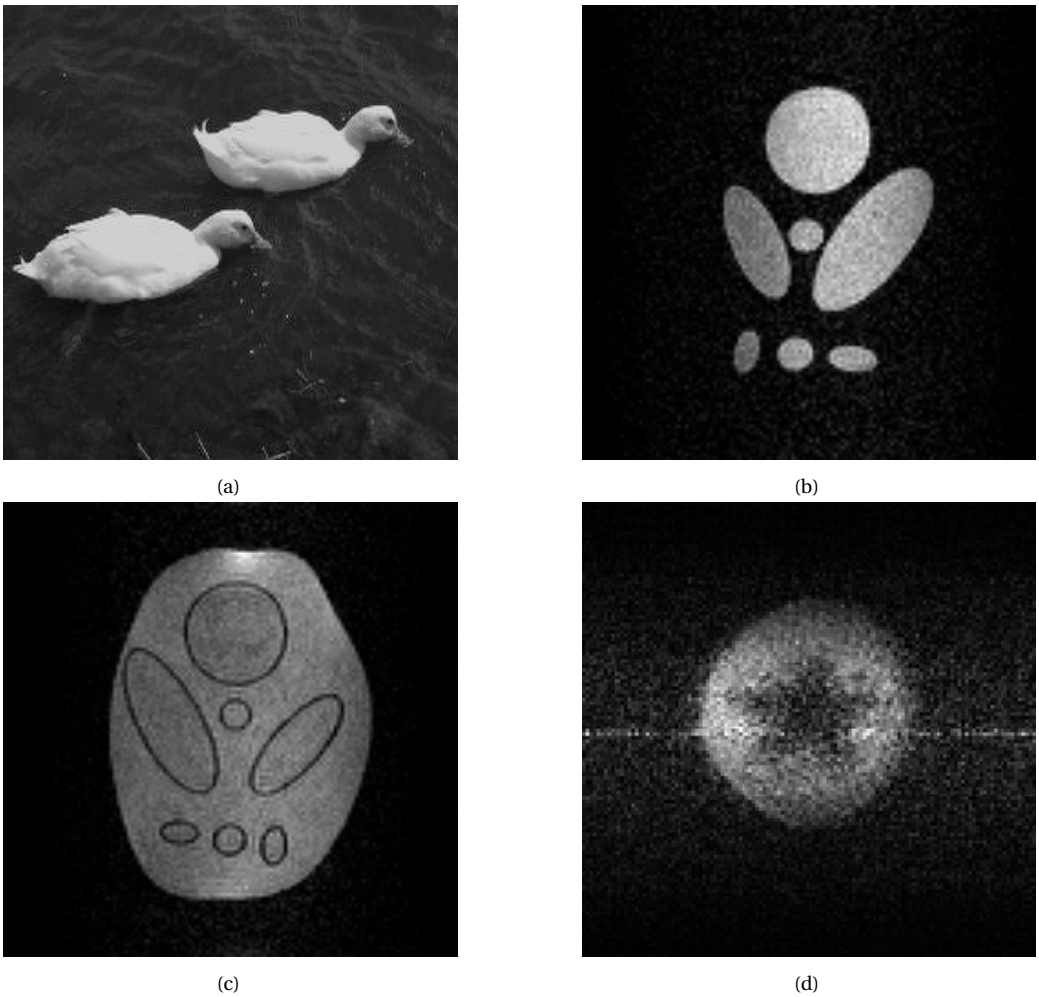

(a) (b) (c) (d)

Figure 5.2: Images and scans used for filtering, enhancement and segmentation.

In this report, four different images/scans will be used for testing the implemented algorithms. First image is presented in Figure 5.2a and was taken from the Weizmann dataset [46]. The second and third images (Figure 5.2c and Figure 5.2b) are scans of $3D$-printed physical phantoms [47] modeled after the Shepp-Logan phantom that serves as a model of a human head for testing imaging techniques [48]. Finally, the last image (Figure 5.2d) is an MRI scan of a papaya.

5.2.1. Low-field MRI Scans Obtained at MUST

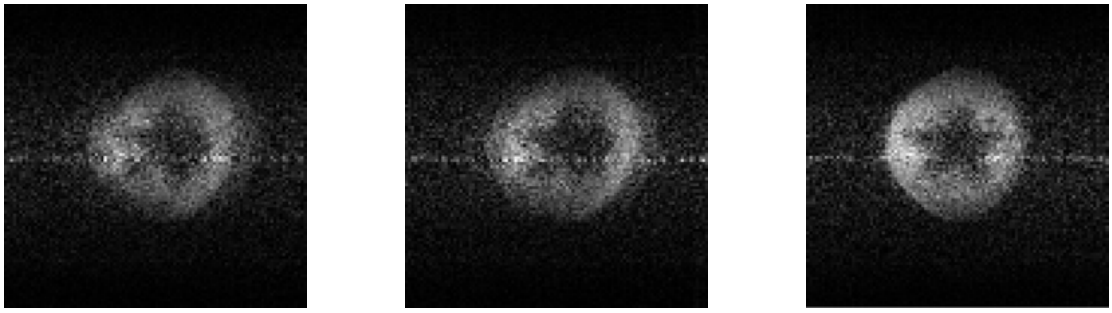

(a) (b) (c)

(d) (e)

Figure 5.3: Scans of a sample object (papaya) obtained with a low-field MRI system for varying values of RF amp and RF duration: (a) `rf_amp` =0.37, `rf_dur` = 300; (b) `rf_amp` = 0.40, `rf_dur` = 250; (c) `rf_amp` = 0.40, `rf_dur` = 300; (d) `rf_amp` = 0.40, `rf_dur` = 350; (e) `rf_amp` = 0.45, `rf_dur` = 300

In June, 2023 a work trip to Mbarara, Uganda took place. During this trip, we managed to conduct some experiments and collect new scans from the MRI system fabricated at MUST (see Figure 1.1a). This is a $46\mu T$ Halbach magnet-based system with a 15cm diameter RF solenoidal coil (Figure 1.1b) and a papaya used a sample (Figure 1.1c). A few ex-

amples of the papaya scans obtained with the MRI system are given in Figures 5.3a to 5.3e. The five cases correspond to different pairs of values of `rf_amp` and `rf_dur`. `rf_amp` is the RF amplitude. The amplitude is intensity of the RF signal generated by the control system and `rf_dur` is the RF duration (see Section 5.1). We observe that the object is shifted for some values of `rf_amp` and `rf_dur`. The level of noise also varies per image.

Apart from the noise present around the object, we can observe a so-called zipper artefact common for MRI [49]. Many parameters are still tuned manually at this stage which affects the quality of the output, so we consider these images as preliminary ones and expect later scans to be of better quality.

Additional scans that were obtained at MUST, but were not used for testing in this report, can be found in Appendix A.

6

Results

All the algorithms were implemented in modern Fortran programming language and tested on the data set described in Chapter 5. In this chapter the results are presented and discussed.

6.1. Two-step Segmentation Approach

This section presents the results of testing the two-step segmentation approach which was discussed in Chapter 4. The following parameters of filtering technique are chosen manually for each image: the fidelity parameter η, the diffusion power d_p, the diffusion parameter K (Equation 2.10, Equation 2.11). For the DPCG method, diagonal scaling is chosen as a preconditioner [32]. Subdomain deflation is applied with the number of subdomains in each direction equal to 8. Next, the maximum number of clusters $n_{\text{cl.}}$ and n_b are adjusted. The latter defines whether background removal (Section 3.3) and morphological closing (Equation 3.13) need to be applied to the filtered image:

$$n_b = -1 \Rightarrow \text{no background removal,} \tag{6.1}$$

$$n_b = 0 \Rightarrow \text{background removal applied,} \tag{6.2}$$

$$n_b \geqslant 1 \Rightarrow \text{background removal applied and closing with a SE of the size } n_b \times n_b \text{ performed.} \tag{6.3}$$

Moreover, if the image is equalized using adaptive histogram equalization (AHE), the number of patches in each direction (n_x and n_y) has to be chosen.

Figures 5.3b to 5.3d do not have ground truth (GT) segmentation, therefore, manual segmentation of the initial scans was carried out with the use of ITK-SNAP [50]. The results of this manual segmentation together with the GT of Figure 5.3a are presented in Figure 6.1.

(a) (b) (c) (d)

Figure 6.1: (a) GT segmentation of Figure 5.3a. (b)-(d) Manual segmentations of Figures 5.3b to 5.3d.

There exist various criteria to assess the quality of segmentation if GT is available. We will use `imabsdiff` *MATLAB* function to compute the absolute differences of the GT and the segmented image and compute the percentage of pixels that were not assigned correctly. When the images do not have the GT, we have to compare the results visually. Some of the inaccuracies in segmentation are marked with red boxes and the improvements are highlighted with yellow boxes.

Results of the two-step approach tested on Figure 5.3a are given in Figure 6.2, 6.4. In the second case, we added Gaussian noise with zero mean and variance of 0.01 to the raw image. All the parameters were kept the same in both cases apart from n_b. It had to be increased to get rid of the background noise. The Gaussian noise was successfully removed by the first step as observed in Figure 6.2b. Both segmentations have small details along the contours that can be further improved. For instance, front parts of the beaks are cut and that can be explained by the small difference in their intensity values and the intensity of the background (the water in this case). Nevertheless, Figure 6.2c , 6.4c show similar results to Figure 6.1a. According to Figure 6.3, only 1.06% and 2.34% of the pixels were not assigned correctly in 6.2c and 6.4c respectively.

(a) (b) (c)

Figure 6.2: (a) Raw image. (b) Filtered image with the parameters $d_p = 0.01, \eta = 8 \cdot 10^2, K = 0.7$ used. (c) Segmented image with the parameters $n_{\text{cl.}} = 1, n_b = 3$ without HE.

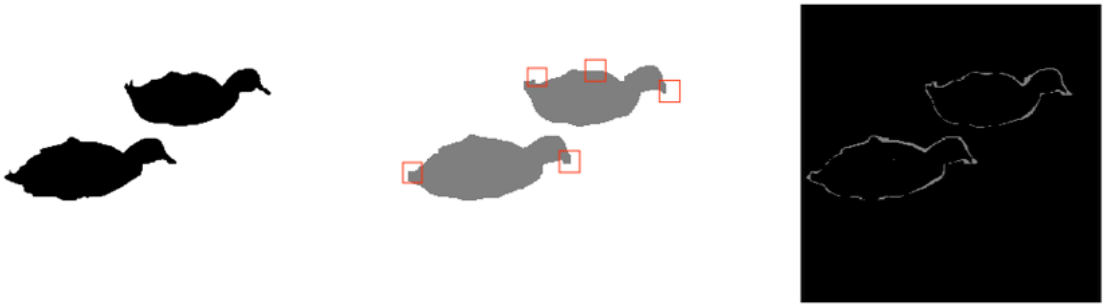

(a) (b) (c)

Figure 6.3: (a) GT. (b) Segmented image 6.2c. (c) Absolute difference between the GT and the segmented image.

(a) (b) (c)

Figure 6.4: (a) Raw image with added Gaussian noise with zero mean and variance 0.01. (b) Filtered image with the parameters $d_p = 0.01, \eta = 8 \cdot 10^2, K = 0.7$ used. (c) Segmented image with the parameters $n_{\text{cl.}} = 1, n_b = 6$ without HE.

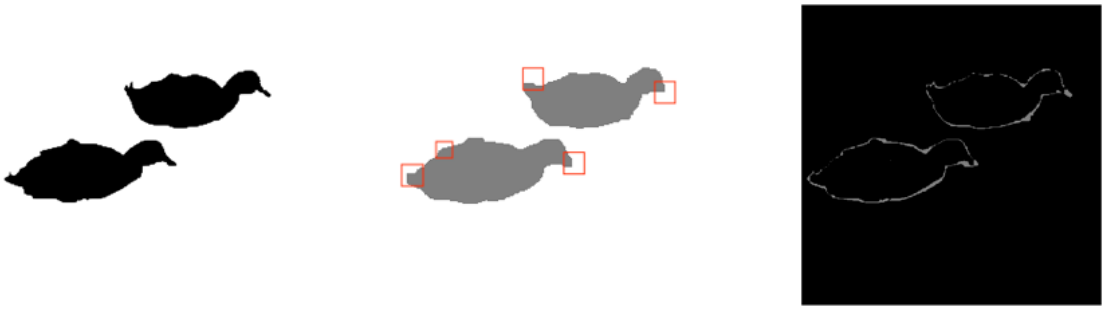

(a) (b) (c)

Figure 6.5: (a) GT. (b) Segmented image 6.2c. (c) Absolute difference between the GT and the segmented image.

Next, we applied the approach to Figure 5.3b. After filtering, a smooth image was obtained (see 6.6b). Final segmented image 6.6c has two types of inaccuracies:

- An intensity peak that, after the background removal is performed, is not assigned to the only cluster;
- Pixels in the central part of the image that were not removed by morphological closing, possibly due the small distance between the objects.

(a) (b) (c)

Figure 6.6: (a) Raw image. (b) Filtered image with the parameters $d_p = 0.01, \eta = 8 \cdot 10^2, K = 1$ used. (c) Segmented image with the parameters $n_{\text{cl.}} = 1, n_b = 1$ without HE.

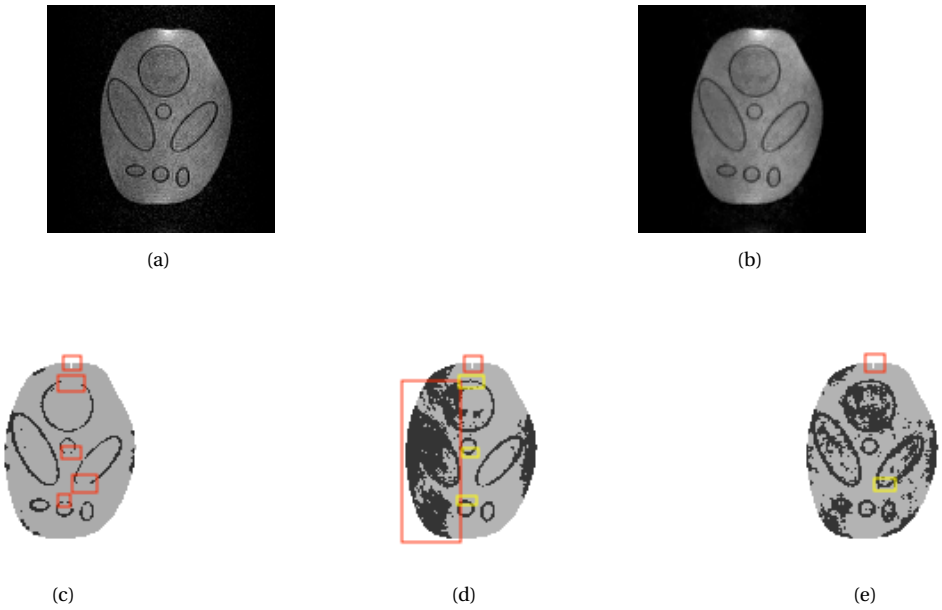

(a) (b)

(c) (d) (e)

Figure 6.7: (a) Raw image. (b) Filtered image with the parameters $d_p = 0.01, \eta = 8 \cdot 10^2, K = 0.2$ used. (c)-(e) Segmented image with the parameters $n_{\text{cl.}} = 2, n_b = 1, n_x = 8, n_y = 1$ in three cases: without HE, with global HE and with AHE.

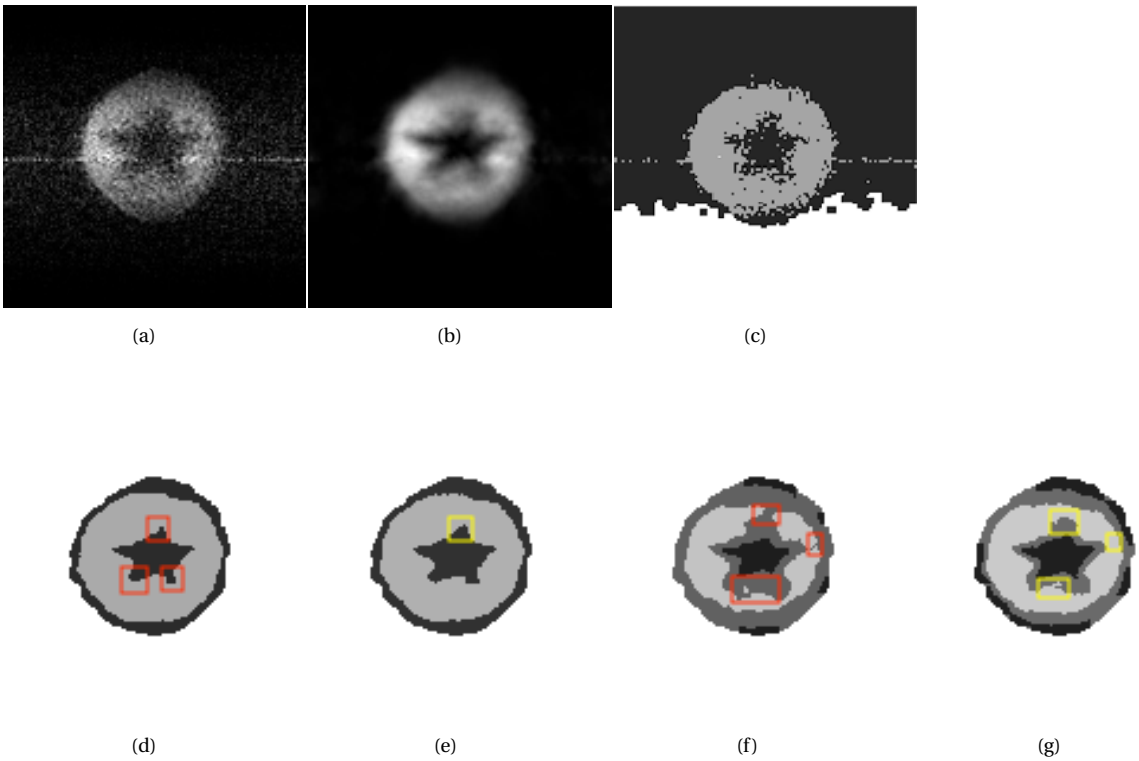

(a) (b) (c)

(d) (e) (f) (g)

Figure 6.8: (a) Raw image. (b) Filtered image with the parameters $d_p = 0.01, \eta = 8 \cdot 10^2, K = 1.7$ used. (c) Segmented image with the parameters $\eta = 5 \cdot 10^4, n_{\text{cl.}} = 2, n_b = 1$ without HE. (d)-(e) Segmented image with the parameters $\eta = 8 \cdot 10^2, n_{\text{cl.}} = 2, n_b = 1$ in two cases: without HE and with global HE. (f)-(g) Segmented image with the parameters $\eta = 8 \cdot 10^2, n_{\text{cl.}} = 3, n_b = 2$ in two cases: without HE and with global HE.

In the next example 6.7, enhancement and segmentation of Figure 5.3c were done. There were certain limitations when choosing the parameters for this case: taking higher values of k, d_p would lead to the edges being blurred. Therefore, though filtering technique managed to smooth out the image (6.7b), some noise was still left and can be observed in Figure 6.7c. We again encounter the intensity peak issue as described in the previous example. Moreover, inner contours are not preserved. Using global HE (6.7d) resolves this issue but increases the noise. Finally, in adaptively equalized image (6.7e), the noise is still present but now spread all over the image. We assume that correcting uneven lighting of the initial image can benefit the segmentation result.

We finally move on to discussing the performance of the two-step approach applied to a low-field MRI scan 5.3d. After the first phase was performed, the filtered image 6.8b was obtained. It was then enhanced and segmented with two different combinations of $n_{\text{cl.}}$ and

n_b values. Although we expect the final number of clusters to be equal to 2, in the second case we considered $n_{\text{cl.}} = 3$ to compare the resulted segmentations. While in the first case the star-shaped core's area is smaller than expected, that of the second case is closer to the manually segmented image Figure 6.1d.

We also provide the results of segmentation 6.8c for an image that was filtered with a higher value of the fidelity parameter ($\eta = 5 \cdot 10^4$ compared to $\eta = 8 \cdot 10^2$ in other cases). Background removal process failed, entailing the rest of the errors. This shows the necessity of adjusting the parameters for each object separately at this phase of our research.

6.2. Modified Two-step Segmentation Approach

In this section we discuss a modification of the two-phase approach where a presegmentation step is added to the first phase. Thus, the image is firstly reconstructed, then segmented and finally filtered. The second phase remains unchanged and is performed as described in Chapter 4. It is important to mention that $n_{\text{cl.}} + 1$ is used during presegmentation as we consider background to be a separate additional cluster at that step.

The modified approach applied to Figure 5.3a yields similar results (figs. 6.9 and 6.11) to both manually segmented solution and the solution in Section 6.1. Moreover, taking $n_{\text{cl.}} = 2$ led to more accurate edges in the final segmentation (compare Figure 6.11d and Figure 6.9c). Indeed, only 0.61% of the pixels in Figure 6.11d ended up in a wrong cluster, while that in the case of Figure 6.9c was 1.69% (see Figure 6.10 and Figure 6.12).

Image 6.9c is included to show the effectiveness of morphological closing. While in 6.11c the background noise is still present, in 6.11d it was eliminated by applying closing with a SE of the size 1×1. Figures 6.11e and 6.11f are given as examples of images where the use of histogram equalization worsened the results.

We move on to testing the modified approach on Figure 5.3c. After the first phase was completed, presegmented and filtered image 6.13b was obtained. The advantage of the modified approach in this particular case is that the contrast increases, therefore, the inner contours are better visible in the segmented image 6.13c. However, some of the noise is still preserved. Due to this noise, histogram equalization only deteriorated the result.

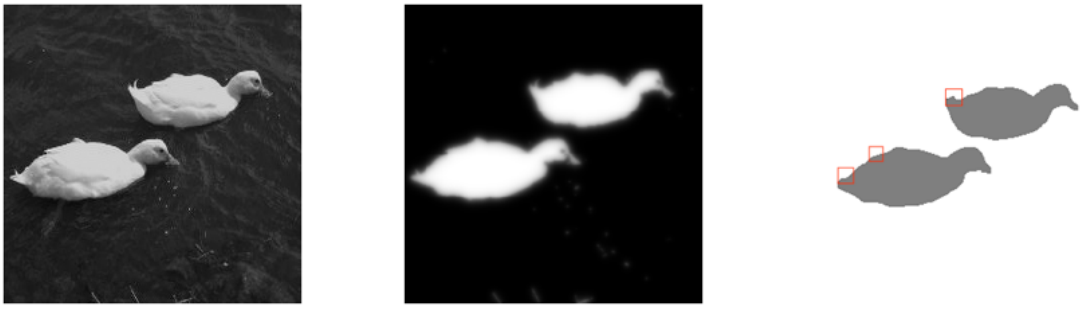

(a) (b) (c)

Figure 6.9: (a) Raw image. (b) Filtered image with the parameters $d_p = 1, \eta = 10^4, K = 1$ used. (c) Segmented image with the parameters $n_{\text{cl.}} = 1, n_b = 2$ without HE.

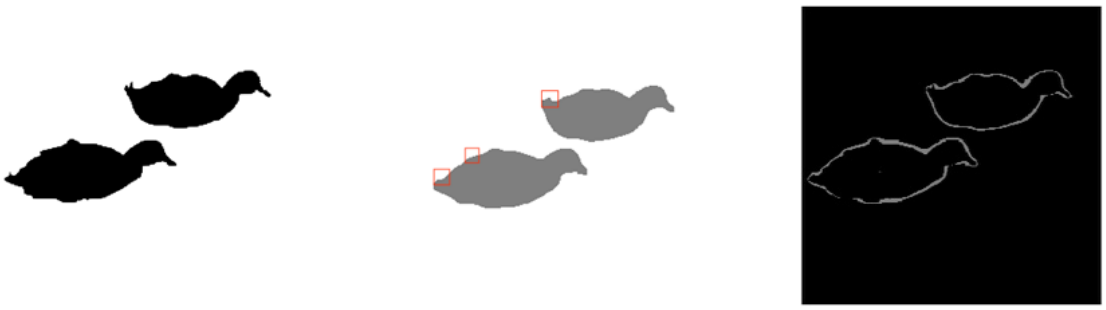

(a) (b) (c)

Figure 6.10: (a) GT. (b) Segmented image 6.9c. (c) Absolute difference between the GT and the segmented image.

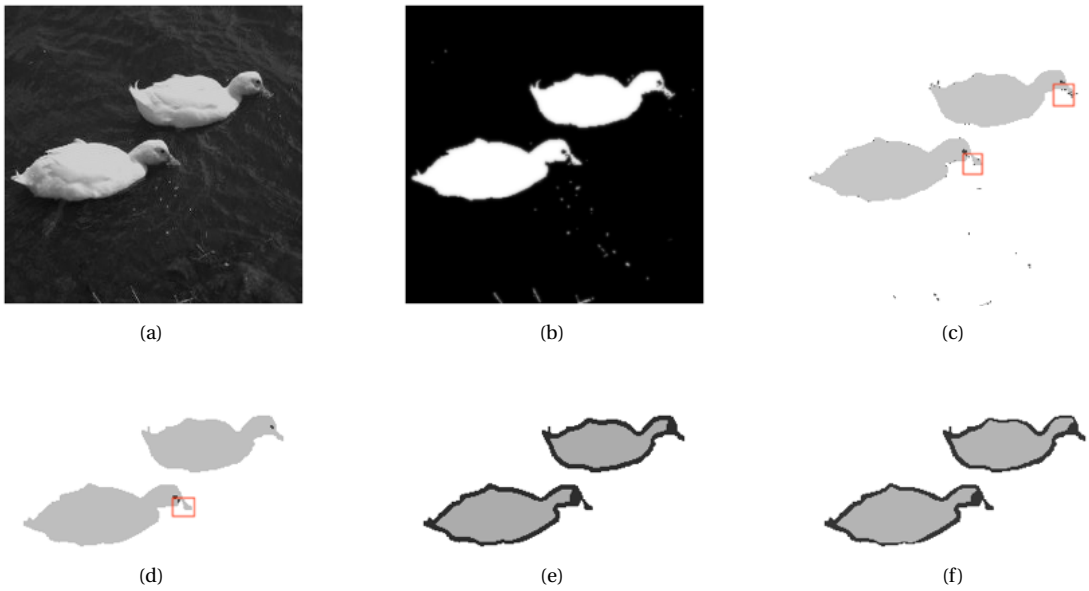

(a) (b) (c)

(d) (e) (f)

Figure 6.11: (a) Raw image. (b) Filtered image with the parameters $d_p = 0.1, \eta = 10^4, K = 1.5$ used. (c) Segmented image with the parameters $n_{\text{cl.}} = 2, n_b = 0$ without HE. (d)-(f) Segmented image with the parameters $n_{\text{cl.}} = 2, n_b = 1, n_x = 16, n_y = 1$ in three cases: without HE, with HE and with AHE.

(a) (b) (c)

Figure 6.12: (a) GT. (b) Segmented image 6.11d. (c) Absolute difference between the GT and the segmented image.

(a) (b) (c) (d)

Figure 6.13: (a) Raw image. (b) Filtered image with the parameters $d_p = 0.01, \eta = 10^3, K = 0.2$ used. (c)-(d) Segmented image with the parameters $n_{\text{cl.}} = 2, n_b = 1$ in two cases: without HE and with HE.

Next, Figure 5.3b was enhanced and segmented. The resulted images can be found in Figure 6.14 and 6.15. All the parameters were the same except for η. We show how the fidelity parameter influenced the first step by comparing Figure 6.14b and Figure 6.15b. While the blurrier image 6.14b led to a result 6.14c similar to the one in 6.6c, the sharper image 6.15b, where the noise was preserved, led to some pixels of the object being considered as background.

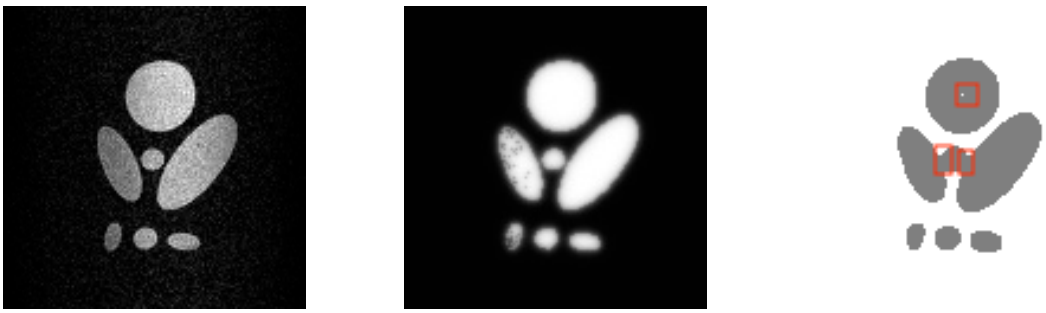

(a) (b) (c)

Figure 6.14: (a) Raw image. (b) Filtered image with the parameters $d_p = 1, \eta = 10^4, K = 1$ used. (c) Segmented image with the parameters $n_{\text{cl.}} = 1, n_b = 1$ without HE.

(a) (b) (c) (d)

Figure 6.15: (a) Raw image. (b) Filtered image with the parameters $d_p = 1, \eta = 10^5, K = 1$ used. (c) Segmented image with the parameters $n_{\text{cl.}} = 1, n_b = 0$ without HE. (d) Segmented image with the parameters $n_{\text{cl.}} = 1, n_b = 1$ without HE.

Finally, we present the results of the modified approach's performance on Figure 5.3d. From the image 6.16b obtained after the first phase, it can be observed that not only were the edges diffused, but the noise also remained after filtering. Consequently, the segmented images figs. 6.16c and 6.16d also exhibit noise and incorrect object contours.

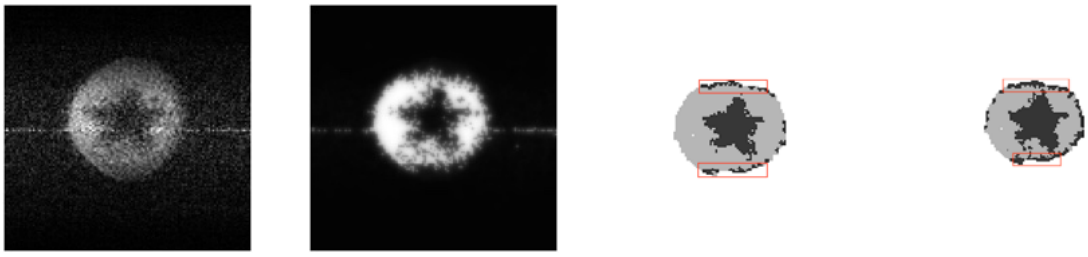

(a) (b) (c) (d)

Figure 6.16: (a) Raw image. (b) Filtered image with the parameters $d_p = 1, \eta = 10^4, K = 1$ used. (c)-(d) Segmented image with the parameters $n_{\text{cl.}} = 2, n_b = 1$ in two cases: without HE and with global HE.

7

Conclusions

In Chapter 1 of this thesis, two research questions have been formulated:

1. Can a two-step PDE-based segmentation approach applied to noisy MRI scans produce reliable results?

2. Can a two-step approach, extended by adding a presegmentation step, yield more accurate segmentation than standard one?

Following the research carried out within this project, we can now answer both questions. It has been shown that the two-step PDE-based segmentation approach tested on both real-life images and MRI scans yields results comparable to the ground truth (GT) and manually performed segmentation. Furthermore, the modified two-step approach produced segmentation results that were similar to those obtained by the standard two-step approach for some of the example scans, while for others, the results were inferior to the standard approach. We find this result to be extremely promising and we believe that the model, developed in this project, followed by subsequent improvements, will find application in real-life medical diagnostics in the future.

First, an in-depth literature review of PDE-based filtering techniques, enhancement methods, and segmentation approaches was conducted. The Nordstrom model, built upon the Perona-Malik model, was selected, and various diffusion coefficients were explored. The Total Variation (TV) diffusion coefficient, complemented with an elastic net term, was applied throughout all the tests. Subsequently, a numerical discretization was then obtained, with the Picard iteration method chosen as the non-linear solver. It was further sped up by combining it with the Deflated Preconditioned Conjugate Gradient method where diagonal scaling was chosen as a preconditioner and deflating matrix was based on domain decomposition.

Next, a spectrum of enhancement and segmentation techniques were introduced and discussed. Background removal, utilizing seeded region growing (SRG), has demonstrated remarkable performance in subsequent experiments. Morphological operations proved highly effective when dealing with noisy images, in particular with low-field MRI scans. Both global histogram equalization (HE) and the newly implemented adaptive HE have proven to be beneficial to the enhancement purposes in some cases. Lastly, the Jenks natural breaks classification method was employed as the primary segmentation technique.

Afterwards, the dataset that was used for testing the enhancement and segmentation techniques, was described. This dataset encompasses not only a real-life image and a Shepp-Logan phantom but also includes low-field MRI scans acquired from the low-field MRI system at Mbarara University of Science and Technology (MUST) during my work visit to Uganda in June. We briefly discussed the physics of MRI to be able to link the physical concepts to the parameters tuned while scanning the objects.

We introduced a two-step PDE-based segmentation approach inspired by the concept presented in [18]. The first phase involves image reconstruction and nonlinear diffusion filtering, discussed earlier. They are combined into an optimization problem that is solved by a single step of the alternating direction method of multipliers (ADMM). The second phase is as follows: solution, obtained in the first phase, is then enhanced by using the aforementioned techniques. Lastly, the enhanced result is partitioned into clusters using the Jenks natural breaks method. This approach has shown to produce reliable segmentation results as can be seen in Section 6.1.

Finally, the standard two-step approach was extended by including presegmentation step in the first phase. As elaborated upon in Section 6.2, the images obtained after the first step have higher intensity contrast. However, this can result in more precise edges, while also introducing greater noise levels in the final segmented images.

The main drawback of our approach lies in the number of parameters that need to be specified individually for each scan. By the time the developed low-field MRI system becomes used for brain imaging, we expect to have found an optimal set of parameters that is suitable for this particular object.

8

Future Research

Despite having achieved promising results in performing segmentation of initially noisy MRI scans, there is always a room for improvements: many different techniques can be incorporated in low-field MRI research.

We recommend exploring alternative methods for solving PDEs: although the standard numerical methods are accurate, they are computationally expensive for complex problems such as nonlinear PDEs. Therefore, physics-informed neural networks (PINNs) [51, 52] can be applied to thhis problem as they have shown to be able to ensure consistency with the physics, as well as being able to extrapolate accurately beyond the available data.

Another aspect to be investigated is the influence of different segmentation-based deflation vectors (e.g. thresholding, region growing) on the accuracy and the efficiency of the DPCG method.

Moreover, combining multiple segmentation techniques may yield better results. Alongside edge detection, SRG, k-means clustering, there also exists such well-known segmentation methods as the Chan-Vese active contour algorithm [53] and morphological extraction of the connected components (ECC). The Chan-Vese algorithm as well as other PDE-based methods is computationally expensive and, therefore, is not widely used. Nowadays, the research mostly focuses on AI-type techniques and neural networks (NNs). However, each method's accuracy varies based on multiple factors. Hence, a comparative analysis of these techniques could identify the most accurate and efficient approach.

Finally, evaluating segmentation performance both when the ground truth (GT) is available and in its absence [54, 55], could constitute a distinct part of the research. It is important to choose suitable evaluation criteria in order to be able to formally assess segmentation performance, going beyond subjective visual assessments.

Bibliography

[1] M. C. Dewan, A. Rattani, R. Mekary, L. J. Glancz, I. Yunusa, R. E. Baticulon, G. Fieggen, J. C. Wellons, K. B. Park, and B. C. Warf. Global hydrocephalus epidemiology and incidence: systematic review and meta-analysis. *Journal of neurosurgery*, 130(4): pp. 1065–1079, 2018.

[2] K. T. Kahle, A. V. Kulkarni, D. D. Limbrick, and B. C. Warf. Hydrocephalus in children. *The lancet*, 387(10020): pp. 788–799, 2016.

[3] M. G. Kartal and O. Algin. Evaluation of hydrocephalus and other cerebrospinal fluid disorders with MRI: An update. *Insights into imaging*, 5(4): pp. 531–541, 2014.

[4] M. Elmaoğlu and A. Çelik. *MRI handbook: MR physics, patient positioning, and protocols*. Springer Science & Business Media, 2011.

[5] W. H. Organization *et al.* Global atlas of medical devices. 2017.

[6] T. O'Reilly, W. M. Teeuwisse, D. de Gans, K. Koolstra, and A. G. Webb. In vivo 3D brain and extremity MRI at 50 mT using a permanent magnet Halbach array. *Magnetic resonance in medicine*, 85(1): pp. 495–505, 2021.

[7] T. O'Reilly, W. Teeuwisse, and A. Webb. Three-dimensional MRI in a homogenous 27 cm diameter bore Halbach array magnet. *Journal of Magnetic Resonance*, 307: p. 106578, 2019.

[8] J. Obungoloch, I. Muhumuza, W. Teeuwisse, J. Harper, I. Etoku, R. Asiimwe, P. Tusiime, G. Gombya, C. Mugume, M. H. Namutebi, *et al.* On-site construction of a point-of-care low-field MRI system in Africa. *NMR in Biomedicine*, p. e4917, 2023.

[9] H. Tang, T. Zhuang, and E. Wu. Realizations of fast 2-D/3-D image filtering and enhancement. *IEEE Transactions on Medical Imaging*, 20(2): pp. 132–140, 2001.

[10] Y. Liu, A. T. Leong, Y. Zhao, L. Xiao, H. K. Mak, A. C. O. Tsang, G. K. Lau, G. K. Leung, and E. X. Wu. A low-cost and shielding-free ultra-low-field brain MRI scanner. *Nature communications*, 12(1): p. 7238, 2021.

[11] V. Lau, L. Xiao, Y. Zhao, S. Su, Y. Ding, C. Man, X. Wang, A. Tsang, P. Cao, G. K. K. Lau, *et al.* Pushing the limits of low-cost ultra-low-field MRI by dual-acquisition deep learning 3D superresolution. *Magnetic Resonance in Medicine*, 90(2): pp. 400–416, 2023.

[12] S. C. Deoni, B. K. Rutt, A. G. Parrent, and T. M. Peters. Segmentation of thalamic nuclei using a modified k-means clustering algorithm and high-resolution quantitative magnetic resonance imaging at 1.5 T. *NeuroImage*, 34(1): pp. 117–126, 2007. ISSN 1053-8119.

[13] S. C. L. Deoni, E. Mercure, A. Blasi, D. Gasston, A. Thomson, M. Johnson, S. C. R. Williams, and D. G. M. Murphy. Mapping Infant Brain Myelination with Magnetic Resonance Imaging. *Journal of Neuroscience*, 31(2): pp. 784–791, 2011. ISSN 0270-6474.

[14] S. C. Deoni, M. M. Bruchhage, J. Beauchemin, A. Volpe, V. D'Sa, M. Huentelman, and S. C. Williams. Accessible pediatric neuroimaging using a low field strength MRI scanner. *NeuroImage*, 238: p. 118273, 2021. ISSN 1053-8119.

[15] D. Fan, N. Gajawelli, A. Paulli, E. Perry, J. Tanedo, S. Deoni, Y. Wang, M. G. Linguraru, and N. Lepore. NEC-NET: segmentation and feature extraction network for the neurocranium in early childhood. In *18th International Symposium on Medical Information Processing and Analysis*, volume 12567, pp. 496–503. SPIE, 2023.

[16] M. Sarracanie, C. D. LaPierre, N. Salameh, D. E. Waddington, T. Witzel, and M. S. Rosen. Low-cost high-performance MRI. *Scientific reports*, 5(1): p. 15177, 2015.

[17] M. H. Mazurek, B. A. Cahn, M. M. Yuen, A. M. Prabhat, I. R. Chavva, J. T. Shah, A. L. Crawford, E. B. Welch, J. Rothberg, L. Sacolick, *et al.* Portable, bedside, low-field magnetic resonance imaging for evaluation of intracerebral hemorrhage. *Nature communications*, 12(1): p. 5119, 2021.

[18] T. Wu, J. Shao, X. Gu, M. K. Ng, and T. Zeng. Two-stage image segmentation based on nonconvex $\ell^2 - \ell^p$ approximation and thresholding. *Applied Mathematics and Computation*, 403: p. 126168, 2021.

[19] G. F. Jenks. The data model concept in statistical mapping. *International yearbook of cartography*, 7: pp. 186–190, 1967.

[20] P. Perona and J. Malik. Scale-space and edge detection using anisotropic diffusion. *IEEE Transactions on pattern analysis and machine intelligence*, 12(7): pp. 629–639, 1990.

[21] J. Weickert *et al.* *Anisotropic diffusion in image processing*, volume 1. Teubner Stuttgart, 1998.

[22] K. N. Nordström. Biased anisotropic diffusion: a unified regularization and diffusion approach to edge detection. *Image and vision computing*, 8(4): pp. 318–327, 1990.

[23] S. T. Acton. Diffusion partial differential equations for edge detection. In *The Essential Guide to Image Processing*, pp. 525–552. Elsevier, 2009.

[24] C. Segall and S. Acton. Morphological anisotropic diffusion. In *Proceedings of International Conference on Image Processing*, volume 3, pp. 348–351 vol.3. 1997.

[25] L. A. Vese and C. Le Guyader. *Variational methods in image processing*. CRC Press, 2015.

[26] F. Catté, P.-L. Lions, J.-M. Morel, and T. Coll. Image selective smoothing and edge detection by nonlinear diffusion. *SIAM Journal on Numerical analysis*, 29(1): pp. 182–193, 1992.

[27] C. R. Vogel and M. E. Oman. Iterative Methods for Total Variation Denoising. *SIAM Journal on Scientific Computing*, 17(1): pp. 227–238, 1996.

[28] R. A. Nicolaides. Deflation of conjugate gradients with applications to boundary value problems. *SIAM Journal on Numerical Analysis*, 24(2): pp. 355–365, 1987.

[29] C. Vuik, A. Segal, and J. Meijerink. An efficient preconditioned CG method for the solution of a class of layered problems with extreme contrasts in the coefficients. *Journal of Computational Physics*, 152(1): pp. 385–403, 1999.

[30] Y. Saad, M. Yeung, J. Erhel, and F. Guyomarch. A deflated version of the conjugate gradient algorithm. *SIAM Journal on Scientific Computing*, 21(5): pp. 1909–1926, 2000.

[31] X. Shan and M. B. van Gijzen. Deflated preconditioned Conjugate Gradient methods for noise filtering of low-field MR images. *Journal of Computational and Applied Mathematics*, 400: p. 113730, 2022.

[32] X. Shan and M. van Gijzen. Deflated Preconditioned Conjugate Gradients for nonlinear diffusion image enhancement. In F.J. Vermolen and C. Vuik, editors, *Numerical Mathematics and Advanced Applications ENUMATH 2019: European Conference, Egmond aan Zee, The Netherlands, September 30-October 4*, pp. 459–468. Springer International Publishing, Cham, 2021. ISBN 978-3-030-55874-1.

[33] R. C. Gonzalez and R. E. Woods. *Digital Image Processing (3rd Edition)*. Prentice-Hall, Inc., USA, 2006. ISBN 013168728X.

[34] R. Adams and L. Bischof. Seeded region growing. *IEEE Transactions on pattern analysis and machine intelligence*, 16(6): pp. 641–647, 1994.

[35] G. Stockman and L. G. Shapiro. *Computer Vision*. Prentice Hall PTR, USA, 1st edition, 2001. ISBN 0130307963.

[36] S. M. Pizer, E. P. Amburn, J. D. Austin, R. Cromartie, A. Geselowitz, T. Greer, B. ter Haar Romeny, J. B. Zimmerman, and K. Zuiderveld. Adaptive histogram equalization and its variations. *Computer Vision, Graphics, and Image Processing*, 39(3): pp. 355–368, 1987. ISSN 0734-189X.

[37] J. MacQueen. Classification and analysis of multivariate observations. In *5th Berkeley Symp. Math. Statist. Probability*, pp. 281–297. University of California Los Angeles LA USA, 1967.

[38] D. Mumford and J. Shah. Optimal approximations by piecewise smooth functions and associated variational problems. *Communications on Pure and Applied Mathematics*, 42(5): pp. 577–685, 1989.

[39] M. de Leeuw den Bouter. *Image Reconstruction for Low-Field MRI*. Ph.D. thesis, Delft University of Technology, 2022.

[40] S. Boyd, N. Parikh, E. Chu, B. Peleato, J. Eckstein, *et al.* Distributed optimization and statistical learning via the alternating direction method of multipliers. *Foundations and Trends in Machine learning*, 3(1): pp. 1–122, 2011.

[41] N. B. Smith and A. Webb. *Introduction to medical imaging: physics, engineering and clinical applications*. Cambridge university press, 2010.

[42] M. E. Ladd, P. Bachert, M. Meyerspeer, E. Moser, A. M. Nagel, D. G. Norris, S. Schmitter, O. Speck, S. Straub, and M. Zaiss. Pros and cons of ultra-high-field MRI/MRS for human application. *Progress in nuclear magnetic resonance spectroscopy*, 109: pp. 1–50, 2018.

[43] J. P. Marques, F. F. Simonis, and A. G. Webb. Low-field MRI: An MR physics perspective. *Journal of magnetic resonance imaging*, 49(6): pp. 1528–1542, 2019.

[44] V. P. Grover, J. M. Tognarelli, M. M. Crossey, I. J. Cox, S. D. Taylor-Robinson, and M. J. McPhail. Magnetic resonance imaging: principles and techniques: lessons for clinicians. *Journal of clinical and experimental hepatology*, 5(3): pp. 246–255, 2015.

[45] A. Berger. How does it work?: Magnetic resonance imaging. *BMJ: British Medical Journal*, 324(7328): p. 35, 2002.

[46] S. Alpert, M. Galun, A. Brandt, and R. Basri. Image Segmentation by Probabilistic Bottom-Up Aggregation and Cue Integration. *IEEE Transactions on Pattern Analysis and Machine Intelligence*, 34(2): pp. 315–327, 2012.

[47] T. O'Reilly and A. Webb. Deconstructing and reconstructing MRI hardware. *Journal of Magnetic Resonance*, 306: pp. 134–138, 2019.

[48] L. A. Shepp and B. F. Logan. The Fourier reconstruction of a head section. *IEEE Transactions on nuclear science*, 21(3): pp. 21–43, 1974.

[49] K. H. Jin, J.-Y. Um, D. Lee, J. Lee, S.-H. Park, and J. C. Ye. MRI artifact correction using sparse+ low-rank decomposition of annihilating filter-based hankel matrix. *Magnetic resonance in medicine*, 78(1): pp. 327–340, 2017.

[50] P. A. Yushkevich, Y. Gao, and G. Gerig. ITK-SNAP: An interactive tool for semi-automatic segmentation of multi-modality biomedical images. In *2016 38th annual international conference of the IEEE engineering in medicine and biology society (EMBC)*, pp. 3342–3345. IEEE, 2016.

[51] R. Mattey and S. Ghosh. A physics informed neural network for time-dependent nonlinear and higher order partial differential equations. *arXiv preprint arXiv:2106.07606*, 2021.

[52] A. J. G. Inda, S. Y. Huang, N. mamolu, R. Qin, T. Yang, T. Chen, Z. Yuan, and W. Yu. Physics Informed Neural Networks (PINN) for Low Snr Magnetic Resonance Electrical Properties Tomography (MREPT). *Diagnostics*, 12(11), 2022. ISSN 2075-4418.

[53] T. F. Chan and L. A. Vese. Active contours without edges. *IEEE Transactions on image processing*, 10(2): pp. 266–277, 2001.

[54] Z. Wang, E. Wang, and Y. Zhu. Image segmentation evaluation: a survey of methods. *Artificial Intelligence Review*, 53: pp. 5637–5674, 2020.

[55] V. V. Valindria, I. Lavdas, W. Bai, K. Kamnitsas, E. O. Aboagye, A. G. Rockall, D. Rueckert, and B. Glocker. Reverse Classification Accuracy: Predicting Segmentation Performance in the Absence of Ground Truth. *IEEE Transactions on Medical Imaging*, 36(8): pp. 1597–1606, 2017.

A

Data Collected in Uganda

In this appendix some additional scans obtained in the MRI lab at MUST are shown (see Figure A.1). A bell pepper, a pineapple, three bottles filled with water/oil and a single bottle filled with oil served as the objects.

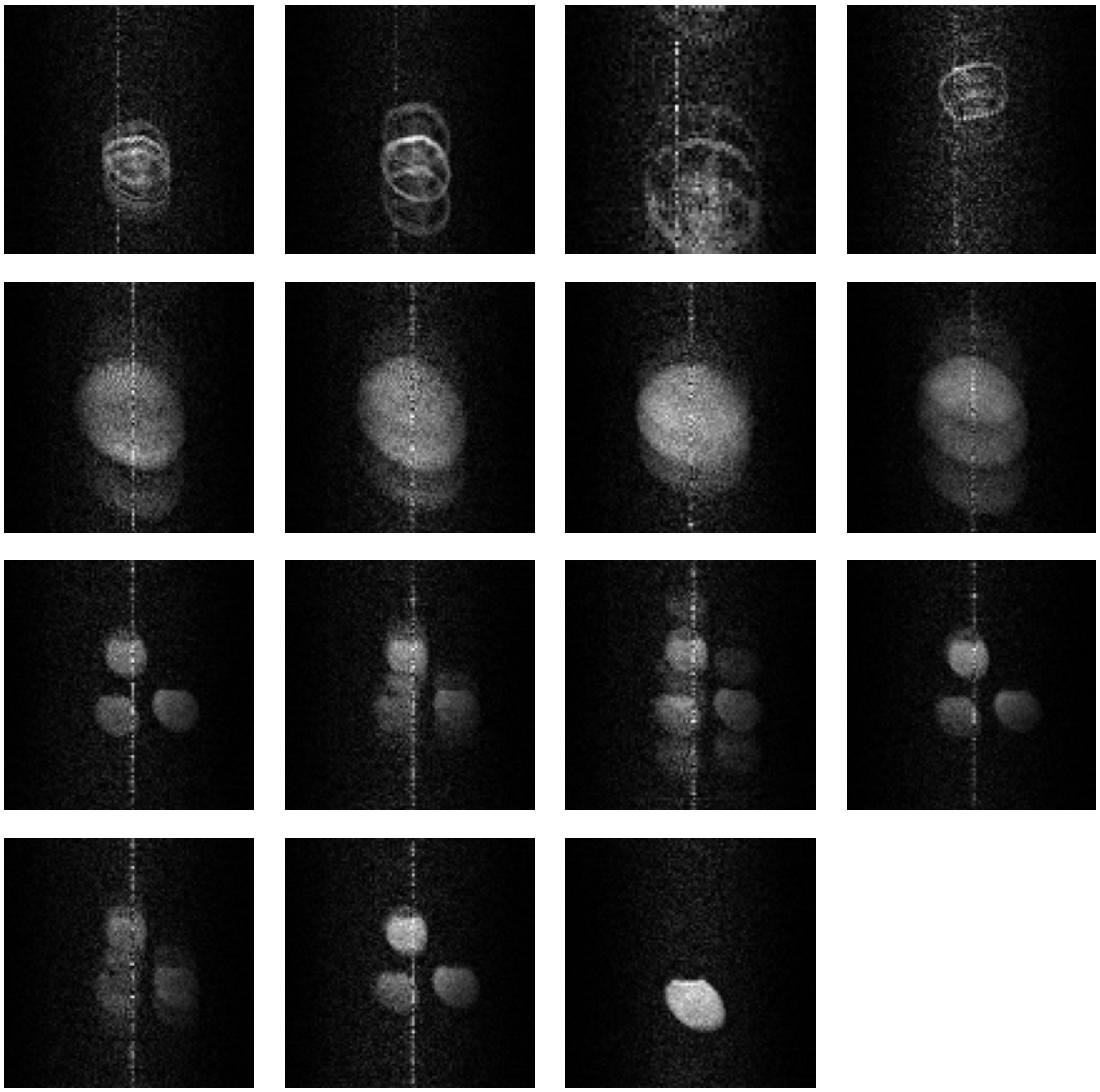

Figure A.1: MRI scans obtained from a low-field MRI system at MUST.

B

Extra Segmentation Results

In this appendix we include additional results (see Figure B.1) of the two-step segmentation approach tested on the papaya scan with a different set of parameters.

(a) (b) (c) (d) (e)

Figure B.1: (a) Raw image. (b) Filtered image with the parameters $d_p = 0.5, \eta = 3 \cdot 10^2, K = 0.5$ used. (c)-(e) Segmented image with the parameters $n_{\text{cl.}} = 2, n_b = 2, n_x = 2, n_y = 2$ in three cases: without HE, with global HE and with AHE.